

A Dynamical Model of the Inner Galaxy

Ralf Häfner, N. Wyn Evans, Walter Dehnen and James Binney

Theoretical Physics, Department of Physics, 1 Keble Rd, Oxford, OX1 3NP

1 February 2008

ABSTRACT

An extension of Schwarzschild’s (1979) galaxy-building technique is presented that, for the first time, enables one to build Schwarzschild models with known distribution functions (DFs). The new extension makes it possible to combine a DF that depends only on classical integrals with orbits that respect non-classical integrals. With such a combination Schwarzschild’s orbits are used only to represent the difference between the true galaxy DF and an approximating classical DF.

The new method is used to construct a dynamical model of the inner Galaxy. The model is based on an orbit library that contains 22 168 regular orbits. The model aims to reproduce the three-dimensional mass density of Binney, Gerhard & Spergel (1997), which was obtained through deprojection of the COBE surface photometry, and to reproduce the observed kinematics in three windows – namely Baade’s Window with $(\ell, b) = (1^\circ, -4^\circ)$ and two off-axis fields at $(8^\circ, 7^\circ)$ and $(12^\circ, 3^\circ)$. The viewing angle is assumed to be 20° to the long axis of the bar and the pattern speed is taken to be $60 \text{ km s}^{-1} \text{ kpc}^{-1}$.

The model fits essentially all the available data within the innermost 3 kpc. The axis ratio and the morphology of the projected density contours of the COBE bar are recovered to excellent accuracy within corotation. The kinematic quantities – the line-of-sight streaming velocity and velocity dispersion, as well as the proper motions when available – are recovered, not merely for the fitted fields at $(1^\circ, -4^\circ)$ and $(8^\circ, 7^\circ)$, but also for three new fields at $(8.4^\circ, -6^\circ)$, $(1.21^\circ, -1.67^\circ)$, and $(-1.14^\circ, 1.81^\circ)$. The dynamical model deviates most from the input density close to the Galactic plane just outside corotation, where the deprojection of the surface photometry is suspect. The dynamical model does not reproduce the kinematics at the most distant window, $(12^\circ, 3^\circ)$, where disk contamination of the data may be severe.

Maps of microlensing optical depth are presented both for randomly chosen stars and for stars that belong to individual components within the model. While the optical depth to a randomly chosen star in Baade’s Window is half what measurements imply, the optical depth to stars in a particular component can be as high as the measured values. The contributions to the optical depth towards randomly chosen stars from lenses in different components are also given.

Key words: Galaxy: structure – stars: kinematics – Galaxy: Centre – methods: numerical

1 INTRODUCTION

We live rather far out in the disc of a spiral galaxy, so studies of the solar neighbourhood do not provide a balanced view of the Galaxy as a whole. It is essential to complement these studies with investigations of the inner Galaxy. This more remote region is hard to study because it is almost completely obscured by dust at optical wavelengths. Consequently, the first indication that ours is a barred galaxy came from 21-cm observations (de Vaucouleurs 1964). It is only in the last few years that a combination of radio-frequency (Binney et al. 1991) and near infrared studies (Blitz & Spergel 1991)

have demonstrated beyond reasonable doubt that the inner Galaxy is dominated by a bar whose nearer end lies at positive longitudes. Evidence from microlensing has also been adduced in favour of a barred inner Galaxy (e.g., Paczyński et al. 1994, Evans 1994), although this remains a controversial matter (e.g., Bissantz et al. 1997, Sevenster et al. 1998).

A promising way to constrain the characteristics of the bar is to combine observations at various wavelengths with theory by trying to construct a *dynamical model* of the inner Galaxy that is compatible with the available data. This is the only true test of our assumptions regarding the Galaxy. Of course, the current observational data are too scanty to

allow us to infer a unique model, and, unsurprisingly, there is controversy as to the viewing angle, length and pattern speed of the Galactic bar (e.g., Binney et al. 1991, Blitz & Spergel 1991, Sevenster et al. 1998). The real value of a dynamical model is that it gives us predictive power and suggests further observational tests to confirm or constrain the structural parameters of the bar. Pioneering studies along these lines include those of Pfenniger & Friedli (1991), Sellwood (1993), Zhao (1996) and Sevenster et al. (1998).

In this paper we build a dynamical model by populating orbits in a given potential. This technique was pioneered by Schwarzschild (1979, 1982, 1993) and further developed by Merritt & Fridman (1996) and Zhao (1996). Schwarzschild's original application of his method was to the building of models of elliptical galaxies in which most of phase space was regular. In general, rotating barred potentials support very considerable numbers of irregular orbits and a straightforward application of Schwarzschild's method is not profitable. In Section 2 we therefore extend Schwarzschild's method in such a way that both regular and chaotic regions of phase space can be populated.

Our model of the inner Galaxy is constrained to fit the three dimensional luminosity density of Binney, Gerhard & Spergel (1997), which was designed to reproduce the infrared data from the COBE satellite. It was recovered by Richardson–Lucy deconvolution of the COBE data, after correction for extinction using a model in which dust is distributed throughout the Galaxy (Spergel, Malhotra & Blitz 1996). The resulting three dimensional density is specified on $59 \times 59 \times 39$ data-cube, corresponding to a box that is 10 kpc on a side and 2.8 kpc thick. Our dynamical model is also constrained to reproduce the kinematic observations in three windows – Baade's Window with $(\ell, b) = (1^\circ, -4^\circ)$ and the two off-axis fields of Minniti et al. (1992) at $(8^\circ, 7^\circ)$ and $(12^\circ, 3^\circ)$. All our constraints are described in Section 3, where particular attention is paid to the best ways of comparing models to kinematic data. To have value, a dynamical model requires a large number of orbits, which are the basic building blocks in Schwarzschild's method. Our orbit library, which contains the density and kinematic contributions of over 23 000 orbits, is described in Section 4. Section 5 discusses the penalty and merit functions used to drive the mass on the orbits towards the desired input density. Our final dynamical model of the inner Galaxy is analyzed in detail in Section 6. There we predict the values of measurable kinematic quantities in several fields near the Galactic centre, describe the model's DF, and analyze the variation of optical depth to gravitational microlensing both with position on the sky and with the Galactic component to which either the source star or the lensing object belongs. Section 7 sums up.

2 EXTENDING SCHWARZSCHILD'S TECHNIQUE

2.1 Splitting the DF

In Schwarzschild's original technique, we calculate N orbits labelled by $i = 1, \dots, N$ in the given potential and determine the fraction p_{ij} of the time that the i th orbit lies in each of the $j = 1, \dots, K$ cells. Let ρ_j^{obs} be the system's original

density in the j th cell with volume V_j . Then we seek the non-negative weights w_i that minimize the discrepancies

$$\Delta_j = V_j \rho_j^{\text{obs}} - \frac{M}{N} \sum_{i=1}^N w_i p_{ij}. \quad (1)$$

Here, the constant factors can be absorbed into the definition of the weights, but we have written them explicitly for later convenience.

So long as the galaxy model is stationary in inertial space or in a frame of reference rotating at constant pattern speed, the Hamiltonian H is an isolating integral of the equations of stellar motion. If the system is axisymmetric, one component of angular momentum, L_z , will also be an isolating integral. Consequently, by Jeans' theorem, any DF that is a function of H , and where appropriate of L_z , will satisfy the collisionless Boltzmann equation (see e.g., Binney & Tremaine 1987). This suggests that we approximate the true DF by a classical DF, $f^{\text{class}}(H)$ or $f^{\text{class}}(H, L_z)$ as appropriate. Since H and L_z are known functions of the conventional phase-space coordinates

$$\mathbf{w} \equiv (\mathbf{r}, \mathbf{p}), \quad (2)$$

we can readily calculate the value of the density or any kinematic quantity to which f^{class} would give rise. Except in special cases, the true DF, f , will depend on non-classical isolating integrals. Therefore we write

$$f(\mathbf{w}) = f^{\text{class}}(H(\mathbf{w}), L_z(\mathbf{w})) + f^{\text{reg}}(\mathbf{w}), \quad (3)$$

where f^{reg} is a function that depends on non-classical isolating integrals. We show below how Schwarzschild's technique can be used to determine simultaneously f^{class} and f^{reg} under the assumption that non-classical isolating integrals exist only along orbits that are regular in the sense that they have three effective isolating integrals. The latter we take to be actions J_i , $i = 1, 2, 3$. For simplicity of exposition we henceforth assume that the only classical integral is H , which is certainly the case for the inner Galaxy. Since DFs that depend on H alone generate isotropic velocity distributions in the appropriate frame of reference, we refer to the component generated by f^{class} as the *isotropic component* and call its DF the isotropic DF, $f^{\text{iso}} = f^{\text{class}}(H)$. All the results below generalize trivially to more general classical DFs.

Note that in our convention $f(\mathbf{w})$ is a probability density and is always normalized to unit phase-space integral inside the box used to fit the density (see below).

2.2 From weights to DF

The key problem involved in representing $f^{\text{reg}} = f - f^{\text{iso}}$ with Schwarzschild's technique, is the determination of the value of the DF that is implied by a given set of weights w_i^{reg} . We solve this problem by using an arbitrary, everywhere positive, correctly normalized probability density $f^{\text{s}}(\mathbf{w})$ to sample points in phase-space. With these points as initial conditions, we integrate along orbits. Then we define

$$\overline{f^{\text{s}}}(\mathbf{J}(\mathbf{w})) = \begin{cases} \lim_{T \rightarrow \infty} \frac{1}{T} \int_0^T dt f^{\text{s}}(\tilde{\mathbf{w}}(t)) & \text{if the orbit is regular,} \\ 0 & \text{otherwise,} \end{cases} \quad (4)$$

where $\tilde{\mathbf{w}}(t)$ is the orbit with initial conditions \mathbf{w} . Constructed thus, $\overline{f^s}(\mathbf{J})$ automatically obeys the collisionless Boltzmann equation. Hence, any distribution function consisting of regular orbits only can be written as

$$f^{\text{reg}}(\mathbf{J}) = w^{\text{reg}}(\mathbf{J}) \overline{f^s}(\mathbf{J}), \quad (5)$$

where $w^{\text{reg}}(\mathbf{J})$ is some weight-function. Moreover, $\overline{f^s}(\mathbf{J})$ gives the relative probability that a regular orbit obtained by sampling phase space according to the probability density $f^s(\mathbf{w})$ will be the orbit with actions \mathbf{J} . The corresponding probability-density for picking the i th regular orbit, is $(2\pi)^3 (N^s/N^{\text{reg}}) \overline{f^s}(\mathbf{J}_i)$, where N^s initial conditions gave rise to N^{reg} regular orbits, while the factor of $(2\pi)^3$ accounts for the phase-space volume at constant \mathbf{J} .

The isotropic part of the DF, f^{iso} , is most conveniently represented by a superposition of basis functions $B_i(E_j)$, for example splines,

$$f^{\text{iso}}(\mathbf{w}) = \sum_i w_i^{\text{iso}} B_i(H(\mathbf{w})), \quad (6)$$

such that the complete DF is determined by the set of weights $\{w_i^{\text{iso}}, w^{\text{reg}}(\mathbf{J})\}$.

2.3 The non-negativity constraint

In irregular regions of phase space, f^{reg} vanishes and the total DF, f , is equal to the isotropic DF, f^{iso} . Hence the latter must be non-negative in irregular regions. By equation (5), the requirement that the total DF be non-negative translates to the following constraint on the weights:

$$w^{\text{reg}}(\mathbf{J}) \geq -\frac{f^{\text{iso}}(H(\mathbf{J}))}{\overline{f^s}(\mathbf{J})} = -\frac{\sum_i w_i^{\text{iso}} B_i(H(\mathbf{J}))}{\overline{f^s}(\mathbf{J})} \quad (7)$$

In general, f^{iso} will be everywhere non-negative and this equation allows $w^{\text{reg}}(\mathbf{J})$ a limited degree of negativity.

The physical implication of an orbit having a negative weight is this. Frequently, both regular and irregular orbits exist at a given value of H . In a three-dimensional system, irregular orbits tend to Arnold diffuse over much of the phase-space hypersurface of constant H . They are, however, rigorously excluded from regions of the hypersurface that are occupied by regular orbits. The isotropic part of the DF may assign non-zero density to irregular orbits at some value of H when the total phase-space density, f , in some regular region of the same energy is negligible. In such a case the weights of the regular orbits would approximately satisfy the equality condition in equation (7). Hence, regular orbits can be important even if no stars are on them by virtue of their ability to exclude stars on irregular orbits from subsets of their energy hypersurfaces.

2.4 From observations to weights

To calculate f , the weights $\{w_i^{\text{iso}}, w^{\text{reg}}(\mathbf{J})\}$ must be determined from observational data. Any observable moment, such as the density, is linear in the DF, and can be split into the contributions arising from f^{iso} and f^{reg} . That is

$$\Pi[f] = \int d^6\mathbf{w} f(\mathbf{w}) \widehat{\Pi}(\mathbf{w}) = \Pi[f^{\text{iso}}] + \Pi[f^{\text{reg}}], \quad (8)$$

where $\widehat{\Pi}(\mathbf{w})$ is the function that characterizes the moment in question – see below. The left-hand side of equation (8) is given by observations and the right-hand side is a linear function of the weights. A sufficiently large set of such equations, for different functions $\widehat{\Pi}$, can now be treated as an inverse problem and a standard technique used to recover the weights $\{w_i^{\text{iso}}, w^{\text{reg}}(\mathbf{J})\}$ from the measured values of the left-hand sides.

Since $H(\mathbf{w})$ is a known function, the moments $\Pi[f^{\text{iso}}]$ are straightforward to evaluate (see Section 4.2). Using (5) and the standard identity $d^6\mathbf{w} \equiv d^3\mathbf{J} d^3\boldsymbol{\theta}$, where the θ_i are the angle variables conjugate to the J_i , the moments arising from f^{reg} can be written as

$$\Pi[f^{\text{reg}}] = \int d^3\mathbf{J} w^{\text{reg}}(\mathbf{J}) \overline{f^s}(\mathbf{J}) \int d^3\boldsymbol{\theta} \widehat{\Pi}(\mathbf{w}(\mathbf{J}, \boldsymbol{\theta})). \quad (9)$$

The right part of the right-hand side can be calculated numerically via the time-averaging theorem (e.g., Binney & Tremaine 1987):

$$\overline{\Pi}(\mathbf{J}) \equiv (2\pi)^{-3} \int d^3\boldsymbol{\theta} \widehat{\Pi}(\mathbf{w}) = \lim_{T \rightarrow \infty} \frac{1}{T} \int_0^T dt \widehat{\Pi}(\mathbf{w}(t)). \quad (10)$$

The integral over $d^3\mathbf{J}$ in equation (9) is performed by Monte-Carlo integration employing N^{reg} regular orbits sampled from the probability density to $(2\pi)^3 (N^s/N^{\text{reg}}) f^s(\mathbf{J})$ that was computed above. This yields:

$$\Pi[f^{\text{reg}}] = \frac{1}{N^s} \sum_{i=1}^{N^{\text{reg}}} w_i^{\text{reg}} \overline{\Pi}(\mathbf{J}_i), \quad (11)$$

where w_i^{reg} is the weight of the i th orbit and $\overline{\Pi}_i$ is the time average of $\widehat{\Pi}(\mathbf{w})$ on this orbit. Note that in practice we do not know $w^{\text{reg}}(\mathbf{J})$ but w_i^{reg} , and hence $w^{\text{reg}}(\tilde{\mathbf{w}}_i(t))$, for the sampled orbits only.

As an example of this formalism, consider M_j^{reg} , the contribution from regular orbits to the mass in cell j . In this case we define

$$\widehat{\Pi}_j(\mathbf{w}) = \begin{cases} 1 & \text{if } \mathbf{w} \text{ lies in cell } j, \\ 0 & \text{otherwise.} \end{cases} \quad (12)$$

Then the phase-space integral over $\widehat{\Pi}_j$, i.e. the left-hand side of equation (9), becomes the fraction of the total mass that is in cell j . Here, “total mass” refers only to the mass M_\square inside the box that contains all cells – recall that $f(\mathbf{w})$ is normalized to unit phase-space integral inside that box. Hence, multiplying equation (11) by M_\square we have the mass M_j^{reg} on regular orbits in cell j

$$M_j^{\text{reg}} = \frac{M_\square}{N^s} \sum_{i=0}^{N^{\text{reg}}} w_i^{\text{reg}} p_{ij}^{\text{reg}}, \quad (13)$$

where

$$p_{ij}^{\text{reg}} = \lim_{T \rightarrow \infty} \frac{1}{T} \int_0^T dt \widehat{\Pi}_j(\mathbf{w}_i(t)) \quad (14)$$

is the fraction of the time that the i th regular orbit is in the j th cell. The analogy between this equation and equation (1) is clear.

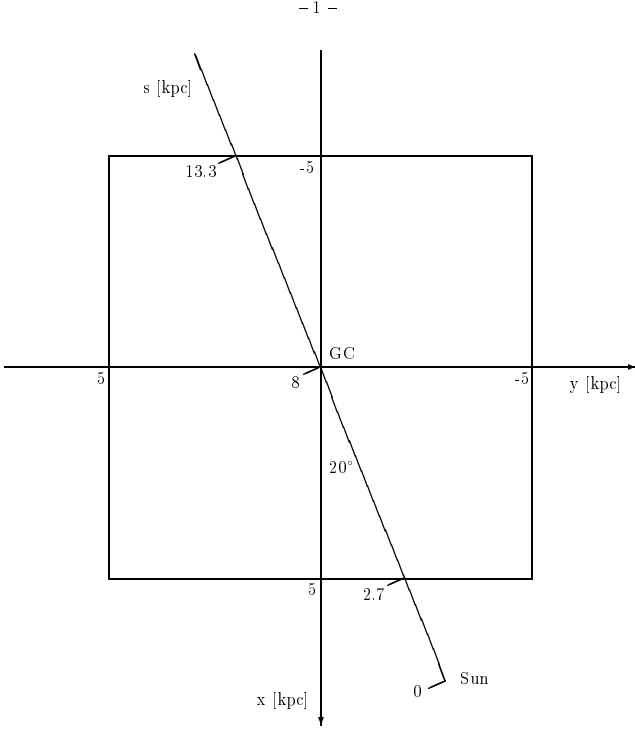


Figure 1. This shows the geometry of the bar in the Galactic plane. The three dimensional luminosity density of Binney et al. (1997) resides in a box that is 5 kpc square in the plane. The viewing angle of the Sun is taken as 20° . The x -axis corresponds to the bar’s major axis, the y -axis is the minor. The intercepts of the line of sight through the Galactic Centre with the box are marked. The bar is rotating in the clockwise direction.

3 APPLICATION TO THE GALAXY

We will be working in a rotating frame of reference, in which the dynamics are governed by the Hamiltonian

$$H(\mathbf{w}) = \frac{1}{2}\mathbf{p}^2 + \Phi(\mathbf{r}) - \boldsymbol{\Omega} \cdot (\mathbf{r} \times \mathbf{p}), \quad (15)$$

where \mathbf{p} is the canonical momentum per unit mass and $\boldsymbol{\Omega}$ is the angular velocity of the bar. Standard manipulations enable us to recast this into the form (e.g., Binney & Tremaine 1987)

$$H(\mathbf{w}) = \frac{1}{2}\mathbf{v}^2 + \Phi_{\text{eff}}(\mathbf{r}), \quad \Phi_{\text{eff}}(\mathbf{r}) = \Phi(\mathbf{r}) - \frac{1}{2}\Omega^2(x^2 + y^2) \quad (16)$$

where \mathbf{v} is the velocity in the rotating frame and Φ_{eff} is the effective potential. The Hamiltonian H , which is an exactly conserved quantity, is also known as Jacobi’s integral E_J .

3.1 The density

As the original density ρ° , we use the three-dimensional model that Binney et al. (1997) obtained by deprojecting the near-infrared COBE surface photometry. The surface photometry employed by Binney et al. had been corrected for absorption by dust by a procedure that is outlined in Spergel, Malhotra & Blitz (1996). The non-parametric Richardson–Lucy algorithm used by Binney et al. is based on the assumption that the density is eight-fold symmetric (with respect to the major, intermediate and minor axes). While this assumption is reasonable enough for the bar it-

self, it causes features like spiral arms to be incorrectly reproduced – see Binney et al. for a discussion of this problem. Both the viewing angle and the pattern speed of the Galactic bar are somewhat controversial (e.g., Binney et al. 1991, Sevenster et al. 1998). For the sake of definiteness, we take the bar’s viewing angle as 20° and the pattern speed as $60 \text{ km s}^{-1} \text{ kpc}^{-1}$. The Sun is assumed to lie at a Galactocentric radius of 8 kpc and 0.014 kpc above the Galactic plane. The circular speed at R_0 is taken to be 200 km s^{-1} . The Sun’s peculiar motion is $(10, 5, 7) \text{ km s}^{-1}$, where the first component is along the line of sight towards the Galactic centre, the second is in the direction of Galactic rotation and the third component points towards the north Galactic pole. In other words, the Sun is moving in towards the Galactic centre, leads the local standard of rest and moves up and away from the Galactic plane (see e.g., Binney & Merrifield 1998). All this means that in the rest frame of the Galaxy with (x, y, z) coordinates aligned with the symmetry axes of the bar, the Sun has phase-space coordinates

$$\begin{aligned} (x, y, z) &= (7.5, 2.7, 0.014) \text{ kpc}, \\ (p_x, p_y, p_z) &= (60.7, -196, 6.98) \text{ km s}^{-1}. \end{aligned} \quad (17)$$

The other coordinate system we frequently use is a heliocentric frame. The line-of-sight distance s and Galactic longitude and latitude (ℓ, b) are the configuration-space coordinates. Velocity space is given by radial or line-of-sight velocity v_{los} , together with the proper motions (μ_ℓ, μ_b) . In this system, the Galactic centre has coordinates

$$\begin{aligned} (s, \ell, b) &= (8, 0, 0) \text{ kpc}, \\ v_{\text{los}} &= -10 \text{ km s}^{-1}, \\ (\mu_\ell, \mu_b) &= (-5.4, -0.18) \text{ mas yr}^{-1} \end{aligned} \quad (18)$$

Note that at the Galactic centre, $1 \text{ mas yr}^{-1} = 37.92 \text{ km s}^{-1}$.

The density plays a dual role in Schwarzschild’s method: it both constrains the weights through equation (40) and, through Poisson’s equation, specifies the potential in which the orbits are calculated. The Galactic density of Binney et al. (1997) comes in two parts. First, inside a box that is 10 kpc on a side and 2.8 kpc thick and whose geometry and position w.r.t. the Sun is shown in Fig. 1, the density is specified on $59 \times 59 \times 39$ grid points. This density distribution was obtained by non-parametric Richardson–Lucy deprojection of the photometry, followed by multiplication by a constant mass to light ratio Υ . Between grid points, the density is evaluated through three-dimensional cubic splines. Outside the box the density is given by an analytic function that is based on the work of Spergel, Malhotra & Blitz (1996):

$$\rho(\mathbf{r}) = \rho_0 [f_b(\mathbf{r}) + f_d(\mathbf{r})] \quad (19)$$

where

$$f_b \equiv f_0 \frac{e^{-a^2/a_m^2}}{(1 + a/a_0)^{1.8}}, \quad (20a)$$

$$f_d \equiv \left(\frac{e^{-|z|/z_0}}{z_0} + \alpha \frac{e^{-|z|/z_1}}{z_1} \right) R_d e^{-R/R_d}, \quad (20b)$$

$$a \equiv \left(x^2 + \frac{y^2}{\eta^2} + \frac{z^2}{\zeta^2} \right)^{1/2} \quad \text{and} \quad R \equiv \sqrt{x^2 + y^2}. \quad (20c)$$

The constants in these equations are as follows: $\rho_0 = 2.05 \times 10^8 \text{ M}_\odot \text{ kpc}^{-3}$ for the L-band, $f_0 = 624$, $a_m = 1.9 \text{ kpc}$, $a_0 = 100 \text{ pc}$, $R_d = 2.5 \text{ kpc}$,

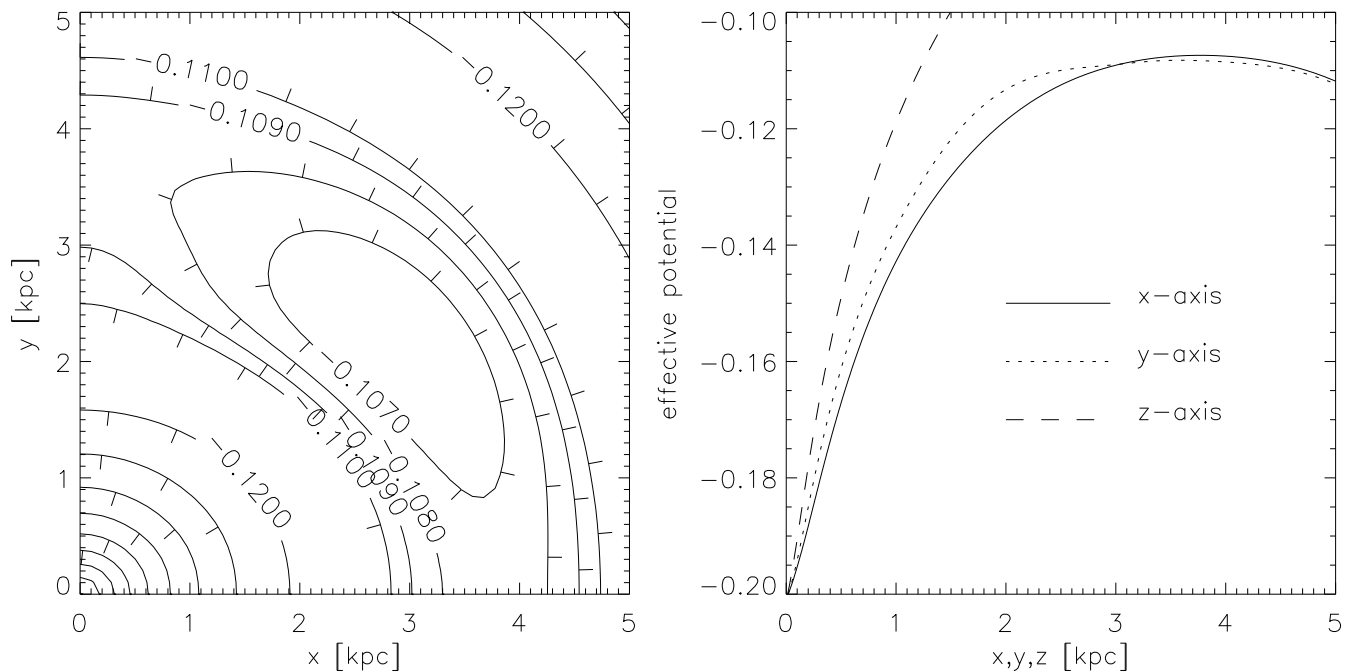


Figure 2. The left panel shows contours of the effective potential in the Galactic plane. The right panel shows the effective potential along the major, intermediate and minor axes. The minimum of the effective potential is at the Galactic Centre, while maxima occur both on the y -axis and at $(x, y) = (\pm 2.9, \pm 2.2)$ kpc. There are saddle points on the x -axis and close to the maxima along the y -axis.

$z_0 = 210$ pc, $z_1 = 42$ pc, $\alpha = 0.27$, $\eta = 0.5$, and $\zeta = 0.6$. Physically, these equations specify an exponential disk, in which the vertical distribution is the sum of two exponentials, and a triaxial bulge that extends to $R \sim 2$ kpc. Since we use the density distribution only at $R > 5$ kpc, the bulge has a negligible impact on our model. box and the density exterior to the box is achieved by setting $\rho = g\rho_{\text{box}} + (1 - g)\rho_{\text{ext}}$, where

$$g \equiv \exp\left[-\frac{s^8}{1 - s^8}\right] \quad 0 \leq s \leq 1 \quad (21)$$

and $s^4 \equiv (x/5 \text{ kpc})^4 + (y/5 \text{ kpc})^4 + (z/1.4 \text{ kpc})^4$. Appendix A describes the technique used to determine the gravitational potential Φ generated by this mass distribution. The interesting features of the potential are conveniently described in the rotating $(\mathbf{r}, \mathbf{v} \equiv \dot{\mathbf{r}})$ frame of the bar. Contours of the effective potential (16) are plotted in Fig. 2. The plot is dominated by a basin whose rim lies at $R \sim 3.8$ kpc. The lowest point on the rim defines the critical value of the potential, $\Phi_{\text{eff}}^{\text{rim}}$. Orbits whose Jacobi energy E_J is smaller $\Phi_{\text{eff}}^{\text{rim}}$ cannot cross the rim. Consequently, orbits belonging to the isotropic component with $E_J < \Phi_{\text{eff}}^{\text{rim}}$ are of two types: those that lie entirely inside the rim, and those that lie outside it. The latter extend to infinity, as do orbits with $E_J \geq \Phi_{\text{eff}}^{\text{rim}}$. Since such unbound orbits are useless for galaxy modelling, f^{iso} is non-zero only for $E_J < \Phi_{\text{eff}}^{\text{rim}}$, and then describes orbits that lie entirely within the rim.

In Fig. 2 a maximum centred on $(2.9, 2.2)$ kpc is conspicuous. The potential's other stationary points are the Lagrange points L_1 to L_5 that were first identified in the context of the restricted three body problem. $L_{1,2,3}$ lie along the x -axis, with L_1 being at the Galactic Centre and $L_{2,3}$ opposite each other at $x \approx \pm 3.7$ kpc, while $L_{4,5}$ lie on the y -axis at $y \approx \pm 3.5$ kpc.

3.2 The kinematics

3.2.1 The selection function

The main problem when observing stars in the bulge is obscuration. This problem is worst within the Galactic plane, and a relatively unobscured optical view at the Galactic centre is only possible in a very few windows, the most famous of which is Baade's Window at $(\ell, b) = (1^\circ, -4^\circ)$.

To compare observational data with a dynamical model, careful thought has to be given to the selection criteria applied to obtain the sample of observed stars. The selection function $\epsilon(s, M)$ is the probability that a star of absolute magnitude M that lies at heliocentric distance s is included in the sample. Unhappily, for many published surveys $\epsilon(s, M)$ is hard to determine. If a survey contains all stars brighter than the limiting magnitude m_{max} and fainter than some cutoff magnitude some magnitude m_{min} , the function $\epsilon(M, s)$ is given by

$$\epsilon(M, s) = \begin{cases} 1 & : m_{\text{min}} < M + 5 \log \frac{s}{10 \text{ pc}} + \gamma s < m_{\text{max}} \\ 0 & : \text{otherwise} \end{cases} \quad (22)$$

where γ is the differential extinction in magnitudes per unit distance. Direct observations of stars and their colour excess yield the total extinction A in certain windows, but γ itself is only available from three-dimensional dust-models whose reliability is uncertain. Even if a dust model fits the dust distribution well when the latter is averaged over some scale, it will be inaccurate at individual points because extinction within the disk is very patchy. Therefore, in equation (22) we use the measured total extinction A rather than the differential extinction γ of a model – since most extinction lies in a foreground screen close to the Sun, this procedure should

not give rise to large errors. To allow for the patchiness of extinction, we treat A as a Gaussian random variable.

If the $\phi(M)$ is the stellar luminosity function, then the general selection function $\epsilon(s)$

$$\epsilon(s) = \int dM \phi(M) \epsilon(M, s), \quad (23)$$

gives the probability that a star at distance s that has unknown absolute magnitude will be included in a survey. Combining the last two equations, we obtain the family of generic selection functions that we will use:

$$\epsilon(s) = \frac{1}{\sqrt{2\pi\sigma_A^2}} \int dA e^{-A^2/2\sigma_A^2} \times \int_{m_{\min}-A-5\log[s/10\text{pc}]}^{m_{\max}-A-5\log[s/10\text{pc}]} dM \phi(M). \quad (24)$$

The samples in the bulge are normally dominated by giant stars. Each type of star (e.g., K giants or M giants) may be considered to have a relatively narrow band of intrinsic luminosities M that is well-modelled by a Gaussian

$$\phi(M) = \frac{1}{\sqrt{2\pi\sigma_M^2}} \exp\left[-\frac{(M - M_{\text{int}})^2}{2\sigma_M^2}\right]. \quad (25)$$

Here, the average intrinsic luminosity M_{int} and dispersion σ_M vary according to stellar type.

3.2.2 The fitted windows

The kinematic data are fitted in three windows. These are Baade's Window and the two off-axis windows studied by Minniti et al. (1992) at $(\ell, b) = (8^\circ, 7^\circ)$ and $(12^\circ, 3^\circ)$. These windows are chosen because the selection criteria seem reasonably clear-cut and reproducible.

Baade's Window has been studied extensively in the visible wave-band and it is the only one for which proper-motion data are available. Sharples, Walker & Cropper (1990) measured line-of-sight velocities for an unbiased sample of 239 late-type M giants. The stars were divided into two groups which show different kinematics. The first group contains 14 bright stars ($I \leq 11.8$) with a relatively small velocity dispersion of $71_{-11}^{+20} \text{ km s}^{-1}$. They are believed to be either in the outer part of the bulge on the solar side, or foreground disk giants, or younger, more massive asymptotic giant-branch stars. The second group, of fainter stars, is attributed to the bulge itself. Sharples et al. argue that this group can be considered complete. The velocity dispersion is considerably higher at $113_{-5}^{+6} \text{ km s}^{-1}$. The mean velocity is $4 \pm 8 \text{ km s}^{-1}$. The value of $113_{-5}^{+6} \text{ km s}^{-1}$ for the line-of-sight velocity dispersion seems to be very robust as other studies find similar values (Rich 1988). This dataset is modelled with one of the generic selection functions introduced in equation (24) with parameters $I_{\text{max}} = 13.4$ and $I_{\text{min}} = 11.8$. The mean extinction $A_I = 0.87$ and its dispersion $\sigma_A = 0.1$ are estimated from Table 3.21 in Binney & Merrifield (1988).

Spaenhauer, Jones & Whitford (1992) conducted the first, and so far only, survey of stars in Baade's Window that measured proper motions rather than just line-of-sight velocities. They compared plates taken at epochs that are 20 years apart and selected 800 stars with $B - V > 1.4$. These

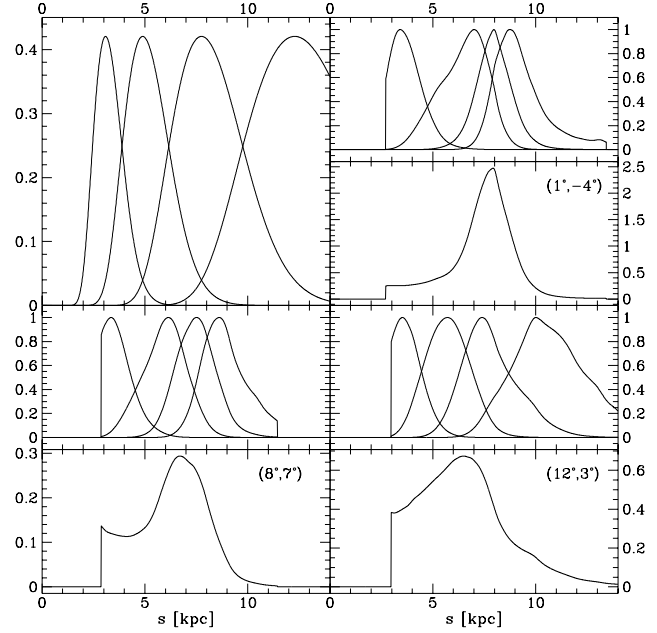


Figure 3. **Top left:** A set of selection functions defined by $m_{\min} = m_{\max} - 1$, $M_{\text{int}} = 0$, $A = 0$, $\sigma_M = 0.5$ and $\sigma_A = 0.1$. m_{\max} is taken to be 13, 14, 15 and 16, respectively. **Top right, bottom left, bottom right:** Two panels are shown for each of the windows at $(1^\circ, -4^\circ)$, $(8^\circ, 7^\circ)$, and $(12^\circ, 3^\circ)$, respectively. The upper panel shows the probability of finding a star at distance s in a given sample while the panel on lower panel shows the density along the line of sight. The sharp cut-off occurs when the edge of the box is reached.

Table 1. The parameters used in the section functions for the data-sets provided by Sharples et al. (1990), Spaenhauer et al. (1992) and Minniti et al. (1992).

(ℓ, b)	m_{\max}	m_{\min}	A	σ_A	m_{int}	σ_M	Ref
$(1^\circ, -4^\circ)$	13.4	11.8	0.87	0.1	-2.75	1.0	Sh
$(1^\circ, -4^\circ)$	17.5	16	1.8	0.2	1.3	1.0	Sp
$(8^\circ, 7^\circ)$	16.5	12	1.5	0.5	-1.5	1.0	M
$(12^\circ, 3^\circ)$	16.5	12	1.5	0.5	-1.5	1.0	M

The first column gives the Galactic coordinates of the window. The next two columns report the faint m_{\max} and bright m_{\min} cut-offs used in the selection function. The fourth and fifth columns give the mean extinction A and its dispersion σ_A . The mean intrinsic magnitude M_{int} and its dispersion σ_M for the luminosity function of the sample are reported in columns six and seven. These refer to the wave-bands in which the observations are taken. The last column is the mnemonic for the window: Sh for Sharples et al., Sp for Spaenhauer et al. and M for Minniti et al.

are almost entirely K and M giants. Out of these 800 stars, 371 were excluded due to overcrowding or because they were too faint. Stars between $B = 17$ and $B = 19$ (roughly) are included. Spaenhauer et al.'s sampling seems best-reproduced by making the following assumptions about the generic selection function: $V_{\text{max}} = 17.5$, $V_{\text{min}} = 16$, $A_V = 1.8$, $\sigma_A = 0.2$, $M_V = 1.3$ and $\sigma_M = 1.0$. It should be noted that neither V_{max} nor V_{min} are hard limits but rather soft boundaries derived from the final sample, while the average extinction is taken from Stanek (1996). Spaenhauer et al. used their measured stars to define the reference frame and so their

means in the proper motions are intrinsic. Only the dispersions in the proper motions – namely $\sigma_\ell = 3.2 \pm 0.1 \text{ mas yr}^{-1}$ and $\sigma_b = 2.8 \pm 0.1 \text{ mas yr}^{-1}$ – carry dynamical meaning.

Finally, Minniti et al. (1992) studied stars in two off-axis fields, namely $(\ell, b) = (8^\circ, 7^\circ)$ and $(12^\circ, 3^\circ)$. Stars with $R \leq 16.5$ were pre-selected. Out of these only the reddest were taken. The limits in colour were chosen to correspond to the locus of K stars. They estimate that in the two fields ~ 10 and ~ 30 per cent are disk stars. The peculiar motion of the Sun is assumed to be 15.4 km s^{-1} towards $(\ell, b) = (51^\circ, 23^\circ)$. The results are $v_{\text{los}} = 45 \pm 10 \text{ km s}^{-1}$, $\sigma_{\text{los}} = 85 \pm 7 \text{ km s}^{-1}$ for the first field, and $v_{\text{los}} = 77 \pm 9 \text{ km s}^{-1}$, $\sigma_{\text{los}} = 68 \pm 6 \text{ km s}^{-1}$ for the second field. When comparing the predictions of our model with the Minniti et al. data, the following generic selection function is used: $R_{\text{max}} = 16.5$, $R_{\text{min}} = 12$, $A_R = 1.5$ and $\sigma_A = 0.5$. The mean intrinsic magnitude of the K stars is taken as $M_R = -1.5$. The mean extinction A_R is merely a crude estimate and is open to debate. The parameters used in the generic selection functions are listed in Table 1 for all the three windows.

As an illustration of the generic selection functions, we plot an example in Fig. 3. These selection functions are of one magnitude width. In other words, $m_{\text{max}} = m_{\text{min}} - 1$. The top left panel shows the selection functions plotted against heliocentric distance. The top right, bottom left and bottom right panels are for the three windows $(1^\circ, -4^\circ)$, $(8^\circ, 7^\circ)$, and $(12^\circ, 3^\circ)$, respectively. In each case, the upper figure shows the number of stars $n(s)$ picked up at a heliocentric distance s , namely

$$n(s) \propto \epsilon(s) \rho(s) s^2, \quad (26)$$

and the lower figure shows the density along the line of sight. The important point is that the selection function has a crucial influence on the observed kinematics, as it controls where the stars are picked up. As m_{min} is varied from 13 to 16, the observables are dominated by foreground stars, then bulge stars proper, and finally stars lying behind the bulge. In principle, the selection function enables us to probe kinematic structure along lines of sight. Instead of just a single value of a variable such as the line-of-sight velocity dispersion, there is really a function depending on the magnitude cut-off.

4 THE ORBIT LIBRARY

This section is concerned with the numerical implementation of our extension of the Schwarzschild algorithm. The first sub-section discusses the choice of the sampling distribution function, which controls the selection of the regular orbits in the orbit library. The second sub-section discusses the choice of the isotropic component.

In this and subsequent sections, the energy E or the Hamiltonian $H(\mathbf{w}) = E_J$ are given in units of $GM_\odot \text{ kpc}^{-1} \approx (978 \text{ km s}^{-1})^2$, while the unit of the angular momentum is $\sqrt{GM_\odot} \text{ kpc} \approx 978 \text{ kpc km s}^{-1}$ with G denoting Newton's constant of gravity.

4.1 The sampling distribution function

Since we use the isotropic DF to populate the irregular parts of phase space, our orbit library contains only regular orbits.

Figure 4. Histograms of the distribution of normalized Liapunov exponents for orbits within three narrow ranges of values of the Jacobi energy E_J . The total area under each of the curves is normalized to unity. The dotted vertical lines show our division into regular and irregular orbits at these Jacobi energies. Orbits to the left of the dotted line are regular, orbits to the right are irregular.

Regular orbits in a rotating barred potential fill a relatively small volume of phase space around the closed prograde orbits and a rather larger volume around the closed retrograde orbits. We ensure that the sampling distribution f^s is large in these regions by using a sum of products of a density distribution $\rho(\mathbf{r})$ of an ellipsoidal Hernquist model, together with functions $h(\mathbf{p})$ of momentum only:

$$f^s = \sum_{i=1}^3 A_i \rho(\mathbf{r}) h_i(\mathbf{p}). \quad (27)$$

Here, the non-negative numbers A_i may be chosen for convenience subject to the condition $1 = \int d^6 \mathbf{w} f^s$.

In the first component of the sampling distribution f^s , $h_1(\mathbf{p})$ is strongly peaked around the momentum of closed prograde orbits. For the second component, $h_2(\mathbf{p})$ is peaked around the velocity of closed retrograde orbits. For the third component, $h_3(\mathbf{p})$ has a broad peak around $\mathbf{p} = 0$. We refer to these components as the prograde, retrograde and hot components, respectively.

Mathematically, for the hot component, h is given by

$$h_3(\mathbf{p}) = \frac{1}{(2\pi)^{3/2} \sigma_x \sigma_y \sigma_z} \exp \left[-\frac{p_x^2}{2\sigma_x^2} - \frac{p_y^2}{2\sigma_y^2} - \frac{p_z^2}{2\sigma_z^2} \right], \quad (28)$$

where the σ_i are specified by Table 2.

In our coordinate system, the Galactic bar and disk have negative angular momentum (see Fig. 1). We define p_ϕ to be $\hat{\mathbf{e}}_\phi \cdot \mathbf{p}$, (which is not the momentum conjugate to azimuth ϕ but the Cartesian momentum \mathbf{p} resolved in the direction of increasing ϕ) and assume that on prograde orbits $\mathbf{p} \simeq -v_c \hat{\mathbf{e}}_\phi$, while on closed retrograde orbits $\mathbf{p} = v_c \hat{\mathbf{e}}_\phi$, where v_c is defined by

$$v_c(R) = 0.25 \left[1 + \left(\frac{0.1 \text{ kpc}}{R} \right)^{0.2} \right]^{-1}. \quad (29)$$

For the prograde and retrograde components, h is given by

$$h_{1,2} = \frac{1}{(2\pi)^{3/2} \sigma_R \sigma_\phi \sigma_z} \exp \left[-\frac{p_R^2}{2\sigma_R^2} - \frac{(p_\phi \mp v_c)^2}{2\sigma_\phi^2} - \frac{p_z^2}{2\sigma_z^2} \right], \quad (30)$$

where the plus sign is taken for the prograde component, and the minus sign for the retrograde component. Table 2 gives the values of the parameters that appear in equation (30).

The spatial parts of the sampling density (27) are defined by

$$\rho(\mathbf{r}) = \frac{10}{27\pi} \frac{1.5 \text{ kpc}}{m} \left(1 + \frac{m}{1.5 \text{ kpc}} \right)^{-3} \quad (31)$$

with

$$m^2 = x^2 + y^2 + (z/0.4)^2. \quad (32)$$

Orbits are followed for ~ 200 dynamical times. Over this time, the Jacobi energy is conserved to typically one part in

Table 2. The velocity dispersions in km s^{-1} of the three components of the sampling distribution function f^s (27).

Component	σ_R	σ_ϕ	σ_x	σ_y	σ_z
prograde	60	60	-	-	50
retrograde	60	60	-	-	50
hot	-	-	100	100	60

The dispersions, given in km s^{-1} , are used in the sampling function and provide the basis for choosing the orbits in the prograde, retrograde and hot components of the orbit library.

10^6 . Liapunov exponents λ are used to distinguish regular from irregular orbits on the principle that $\lambda = 0$ for a regular orbit. The process of estimating λ is discussed by Udry & Pfenniger (1988). In practice, we extrapolate to infinite time by fitting the estimate $\bar{\lambda}(t)$ obtained by following the orbit for time t to $\bar{\lambda} = \lambda + b/t$. These unnormalized Liapunov exponents are converted to normalized ones by multiplying by the orbital time. This is defined to be the mean time between successive passages through the plane $\dot{y} = 0$. Fig. 4 shows three histograms of values of normalized Liapunov exponents λ_{norm} for orbits in three narrow ranges of E_J . In all three cases, there is a sharp peak around $\lambda_{\text{norm}} = 0$, which corresponds to the regular orbits. After integrating for an infinite time, one might expect all irregular orbits at any one Jacobi energy E_J to be equivalent. Since we only calculate for finite time, the peak corresponding to the irregular orbits is broadened. The dotted vertical lines in Fig. 4 separate the regular and the irregular orbits. In addition to this, we also include all orbits whose Liapunov time is greater than five bar rotation times. This seems reasonable as such orbits do not evolve on the time-scale (~ 100 bar rotation periods) of interest to us.

The prograde sampling function is used to select 200 000 initial conditions. These give rise to only 5 713 regular orbits. Similarly, 100 000 initial conditions selected from the sampling distribution of the hot component give rise to 5 512 regular orbits. Only 50 000 initial conditions selected from the sampling function of the retrograde component give rise to 10 943 regular orbits. The final orbit library contains $N^{\text{reg}} = 22\,168$ regular orbits. The library records the probabilities of each orbit being in any given cell and the time-averaged sampling density.

Fig. 5 shows the density of the library's orbits in a convenient projection of orbit space. In a conventional Lindblad diagram for an axisymmetric galaxy, the angular momentum L_z of orbits is plotted horizontally, and their energy is plotted vertically. The top panel of Fig. 5 is a modified Lindblad plot for our system, in which *orbit-averaged* values of L_z and energy are plotted horizontally and vertically. These averages are effective rather than classical integrals. Since the Hamiltonian satisfies $H = E - \Omega L_z$, the classical integral H is a linear combination, $\langle E \rangle - \Omega \langle L_z \rangle$ of the effective integrals. We choose to plot $\langle E \rangle$ rather than H because the former is a truer guide to an orbit's physical size than the latter. In a classical Lindblad diagram, the allowed region $|L_z| \leq L_c(E)$, where $L_c(E)$ is the angular momentum of a circular orbit of energy E , tapers as one descends to smaller values of E . In Fig. 5 this tapering has been largely suppressed by plotting horizontally not $\langle L_z \rangle$ but $\langle L_z \rangle / L_c$, where L_c is not the angular momentum of a circular orbit,

which does not exist in a barred galaxy, but is defined to be (in the units given above)

$$L_c(\langle E \rangle) = \frac{1}{600} (\langle E \rangle + 0.25)^4. \quad (33)$$

Since the Galactic bar has a negative pattern speed, prograde orbits lie on the left hand side of Fig. 5 and contours of constant H slope from top left to bottom right. The red curve in Fig. 5 is the contour for $H = \Phi_{\text{eff}}^{\text{rim}}$. The region of strong chaos associated with corotation is evident in the white sea that cuts the $\langle E \rangle$ axis between -0.035 and -0.075 . Within this sea there is a long thin island of regularity. The panels marked C1 and C2 show two orbits within this island. One is trapped around the standard maximum of Φ_{eff} at L_4 . The other is trapped around the non-standard maximum of Φ_{eff} at $(\pm 2.9, \pm 2.2)$ kpc. At smaller values of $\langle E \rangle$, a ridge of orbits trapped around the prograde, bar-supporting x_1 family is apparent near the left-hand edge of Fig. 5. The panels marked A, B1 and B2 in the lower half of Fig. 5 show representative orbits from this region. Panel D shows a prograde orbit at the largest value of $\langle E \rangle$ plotted in Fig. 5. This is a typical disk orbit.

On the right-hand, retrograde side of orbit space, orbits of the x_4 family occupy a region of regularity that extends, unbroken, from the smallest to the largest energies. The panels labelled K, L and M show representative orbits from this region.

In Fig. 5, colour shows the density of orbits, while white dots show the orbits themselves. Many sharp chains of dots can be discerned: these mark the paths of stable resonances.

4.2 The isotropic component

The isotropic DF can be conveniently represented as a linear combination of some basis functions – the coefficients in this expansion are the free parameters that then determine f^{iso} . We have employed second-order basis-splines (see e.g., Stoer & Bulirsch 1980). Hence,

$$f^{\text{iso}}(\mathbf{w}) = \sum_{i=1}^{N^{\text{iso}}} w_i^{\text{iso}} B_i(H(\mathbf{w})), \quad (34)$$

where $N^{\text{iso}} = 1000$ and

$$B_i(E_J) = \frac{k_i}{\Delta E_J} \times \begin{cases} E_J - E_{J_{i-1}} & \text{for } E_J \in [E_{J_{i-1}}, E_{J_i}], \\ E_{J_{i+1}} - E_J & \text{for } E_J \in [E_{J_i}, E_{J_{i+1}}], \\ 0 & \text{otherwise.} \end{cases} \quad (35)$$

Here, ΔE_J denotes the grid spacing, taken to be constant, while the k_i are constants that enforce some chosen normalization. The basis functions $B_i(H(\mathbf{w}))$ can be interpreted as building blocks containing all orbits with Jacobi integral $E_J = H(\mathbf{w})$ for which $B_i(E_J) > 0$.

As mentioned in Section 3.1, outside corotation, irregular orbits can escape to infinity. Since these irregular orbits are occupied via f^{iso} , we must restrict f^{iso} to values of E_J of orbits that cannot cross the potential rim at corotation. This means that (i) f^{iso} is non-zero only for $E_J < \Phi_{\text{eff}}^{\text{rim}}$, and (ii) at fixed $E_J < \Phi_{\text{eff}}^{\text{rim}}$ refers only to orbits inside corotation. Thus, strictly speaking equation (34) for f^{iso} contains two Heaviside functions, one ensuring $E_J < \Phi_{\text{eff}}^{\text{rim}}$ and the other $|x| < x_{\text{rim}}$, where $\Phi_{\text{eff}}^{\text{rim}} = \Phi_{\text{eff}}(x_{\text{rim}}, 0, 0)$. For simplicity, we have suppressed these Heaviside functions.

Figure 5. Top panel: The density of orbits in the library of regular orbits is colour-coded, with black the lowest density. Scaled, time-averaged angular momentum is plotted horizontally and time-averaged energy vertically. The red curve is the contour $H = \Phi_{\text{eff}}^{\text{rim}}$, above which orbits are not confined by the Hamiltonian and the isotropic part of the DF, f^{iso} , is set to zero. Individual orbits are marked by white dots. **Lower panels:** representative orbits. The location of each orbit in the top panel is indicated by the letter to the right or the orbit and the $(\langle E \rangle, \langle L_z \rangle)$ coordinates on top of it. Orbits are followed for 200 dynamical times.

Table 3. Labelling of the velocity moments in the merit function.

i	ω_{ji}
1...3	$\langle v_{\text{los}} \rangle, \langle \mu_\ell \rangle, \langle \mu_b \rangle$
4...6	$\langle v_{\text{los}}^2 \rangle, \langle \mu_\ell^2 \rangle, \langle \mu_b^2 \rangle$
7...9	$\langle v_{\text{los}} \mu_\ell \rangle, \langle v_{\text{los}} \mu_b \rangle, \langle \mu_\ell \mu_b \rangle$

Not all these components of the velocity dispersion tensor are available for all the windows. The most complete information is known for Baade’s Window – namely, $v_{\text{los}}, \sigma_{\text{los}}, \sigma_\ell$ and σ_b .

Computing moments of the isotropic DF, f^{iso} , reduces to computing them for the B_i . For the mass density, for example,

$$\rho^{\text{iso}}(\mathbf{r}) = M_\square \sum_i w_i^{\text{iso}} p_i^{\text{iso}}(\mathbf{r}), \quad (36)$$

where

$$p_i^{\text{iso}}(\mathbf{r}) \equiv \int d^3 \mathbf{v} B_i(E_J) = \frac{4\sqrt{2}k_i}{15 \Delta E_J} [D_{i-1}^5 - 2D_i^5 - D_{i+1}^5] \quad (37)$$

with $D_i^2 \equiv E_{Ji} - \Phi_{\text{eff}}(\mathbf{r})$. The k_i are determined by normalizing p_i^{iso} such that

$$1 = \int d^3 \mathbf{r} p_i^{\text{iso}}(\mathbf{r}). \quad (38)$$

This integral over real space is done numerically by the Monte-Carlo method.

5 THE MERIT AND PENALTY FUNCTIONS

The combined mass density of the orbits must match the original density ρ^{obs} used to create the potential (see Section 3.1). To this end we minimize the merit function

$$Q^{\text{den}} = \sum_j \left[\frac{\Delta_j}{\rho_{\text{norm } j}} \right]^2, \quad (39)$$

where the sum extends over all cells and

$$\Delta_j = \frac{M_j^{\text{obs}}}{M_\square} - \left[\sum_{i=1}^{N^{\text{iso}}} w_i^{\text{iso}} p_{ij}^{\text{iso}} + \frac{1}{N^{\text{reg}}} \sum_{i=1}^{N^{\text{reg}}} w_i^{\text{reg}} p_{ij}^{\text{reg}} \right], \quad (40)$$

where $M_\square = 5.18 \times 10^{10} M_\odot$, while M_j^{obs} is the mass contained in the j th cell of our mass model according to BGS. p_{ij}^{iso} is the integral of $p_i^{\text{iso}}(\mathbf{r})$ [equation (37)] over cell j . Because the B_i are normalized to unit phase-space integral, p_{ij}^{iso} is just the probability for a star whose phase-space coordinates are drawn from $B_i(H(\mathbf{w}))$ to be found in cell j at any time. Equivalently, p_{ij}^{reg} , defined by equation (14), is the probability that a star on the i th regular orbit is found

in cell j at any time. The weighting of the cells, $\rho_{\text{norm } j}$, is chosen to be

$$\rho_{\text{norm } j} = \frac{\rho_j^{\text{obs}}}{\sqrt{N_{\text{sam } j}}}, \quad (41)$$

where $N_{\text{sam } j}$ is the number of building blocks contributing to grid cell j . The effect of this weighting scheme is a minimization of relative errors in the density modified by the Poisson error expected from the sampling.

The kinematics of our model are given by the matrix ω_{ji}^{m} with $i=0, \dots, 9$ representing the i th velocity moment in window j , as defined in Table 3. Appendix B gives details of the calculation of the moments. The contribution to the merit function of the kinematic constraints is

$$Q^{\text{kin}} = \sum_j \sum_{i=1}^9 \gamma_{ji} (\omega_{ji}^{\text{m}} - \omega_{ji}^{\text{o}})^2, \quad (42)$$

where γ_{ji} is a weighting matrix and the superscripts m and o refer to the model and observed quantities, respectively. In some windows only a subset of the moments is available. For all three of the constraint windows (described in Section 3.2), line-of-sight velocity v_{los} and dispersion σ_{los} are known. Only in Baade’s Window are the dispersions σ_ℓ and σ_b also available.

The problem posed by the minimization of the merit function is very ill-conditioned, so regularization is necessary. This is achieved by enforcing a smoothness constraint – ‘neighbouring’ orbits should have ‘similar’ weights. A suitable penalty function is the mean-square value of the second derivative of the logarithm of the weights with respect to some distance – this vanishes when the dependence of weights on distance is a power law. For orbits belonging to the isotropic DF, a suitable distance is provided by E_J , and the penalty function reads

$$P^{\text{iso}} = \frac{1}{N^{\text{iso}}} \sum_{i=2}^{N^{\text{iso}}-1} \left[\frac{\ln w_{i-1}^{\text{iso}} - 2 \ln w_i^{\text{iso}} + \ln w_{i+1}^{\text{iso}}}{(\Delta E_J)^2} \right]^2. \quad (43)$$

For the regular orbits, the distance measure is provided by a set of effective integrals (c.f. Merritt & Fridman 1996, Zhao 1996). Specifically, we employ the time averages $I_1 \equiv \langle p_z^2 \rangle$, $I_2 \equiv \langle L_z \rangle$ and $I_3 \equiv \langle E \rangle$ – note that I_3 is the mean orbital energy, not the value of E_J . The penalty function for regular orbits then reads

$$P^{\text{reg}} = \frac{1}{N^{\text{reg}}} \sum_{i=1}^{N^{\text{reg}}} \left[\frac{\ln w_i^{\text{reg}} - \langle \ln w^{\text{reg}} \rangle_{A(i)}}{\langle d \rangle_{A(i)}} \right]^2. \quad (44)$$

Here, $A(i)$ is a neighbourhood of orbit i and $\langle \rangle_{A(i)}$ denotes the average within this neighbourhood. $A(i)$ is defined to

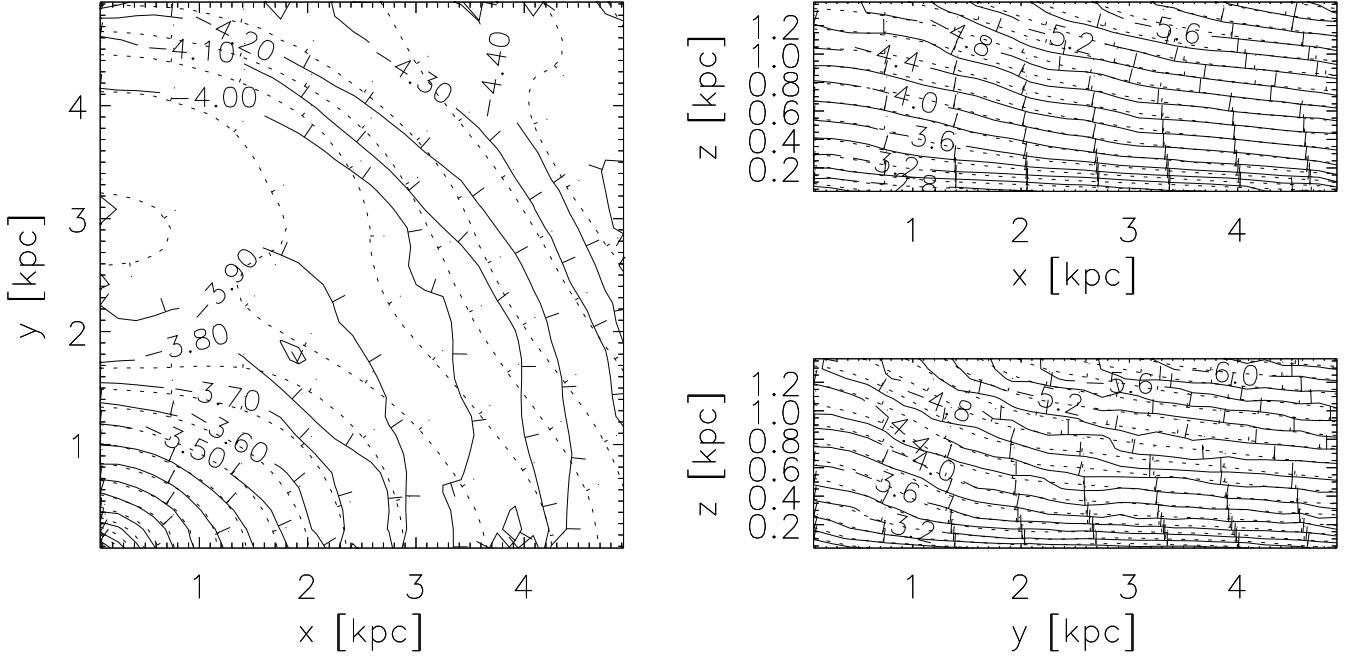


Figure 6. Logarithmic contours of the projected mass in the principal planes of the Binney et al. (1997) model (dotted lines) are compared with those of our dynamical model (full lines). The units are such that the total mass in the $10 \text{ kpc} \times 10 \text{ kpc} \times 2.8 \text{ kpc}$ box is unity.

consist of the 8 orbits closest to orbit i . The distance, d_{ij} , between orbits $i \neq j$ is defined by

$$d_{ij} \equiv \sum_{k=1}^3 \left[\frac{I_{ki} - I_{kj}}{\sigma_{I_k}} \right]^2, \quad (45)$$

where σ_{I_k} is the dispersion of I_k over all the regular orbits.

The final quantity to be minimized, \bar{Q} , is a linear combination of the density and kinematic merit functions, Q^{den} and Q^{kin} , and the penalty functions P^{reg} and P^{iso} . The final numerical factors in this linear combination were chosen as follows. The relative weight for Q^{kin} was chosen to be as small as possible without increasing the deviation from the observed kinematics by more than the observational uncertainty (1σ). Similarly, the relative weight for the penalty functions were chosen as large as possible without worsening the fit to the mass density by more than 2 per cent overall.

To enforce the non-negativity of f , we substitute the weights w_j^{iso} and w_j^{reg} by β_j^{c} and β_j^{r} in the following way:

$$\beta_j^{\text{iso}} = \ln w_j^{\text{iso}} \quad (46a)$$

$$\beta_j^{\text{reg}} = \ln \left[w_j^{\text{reg}} + \bar{f}^{\text{s}}(\mathbf{J}_j)^{-1} \sum_{i=1}^{N^{\text{iso}}} w_i^{\text{iso}} B_i(H(\mathbf{J}_j)) \right]. \quad (46b)$$

Hence, $\beta_j^{\text{reg}} \rightarrow -\infty$ as w_j^{reg} tends to the lowest value compatible with the positivity constraint (7). Minimizing \bar{Q} with respect to $\{\beta_j^{\text{iso}}, \beta_j^{\text{reg}}\}$ always results in a physical model. Unfortunately, two attractive properties of the original optimization problem are lost in the transition from the w 's to the β 's: Q^{den} no longer depends linearly on the variables, and the boundedness of the solution is not guaranteed (as the β 's can diverge).

Due to the great number of orbit weights to be determined, the memory requirement of the adopted optimiza-

tion algorithm must not increase with the number of unknowns faster than linearly. This excludes fast schemes such as non-negative least square fitting (e.g., Zhao 1996). Another popular choice, the iterative Richardson-Lucy method (Newton & Binney, 1984; Statler, 1987), is not applicable to our problem because its kernel is not positive definite. Our final choice fell on the conjugate gradient algorithm (e.g., Stoer & Bulirsch 1980; Press et al. 1988). It satisfies the stringent memory requirements and is an improvement on the steepest descent method in so far as the directions in which it does its line minimizations are conjugate to each other.

6 RESULTS

This section describes our dynamical model of the Milky Way's bar. Section 6.1 describes how the model reproduces the density and kinematic constraints. Section 6.2 provides kinematic predictions of the model, while Section 6.3 discusses the phase-space structure.

6.1 The constraints

6.1.1 The density

The full contours in Fig. 6 show the density of our final dynamical model projected onto the three principal planes. The broken contours show the corresponding projections of the input density of Binney et al. (1997). Overall, the fit between the two density distributions is good, with the average discrepancy $\sim 10\%$. The biggest contribution to this error comes from the innermost two layers of cells close to the Galactic plane, and particularly around corotation on the

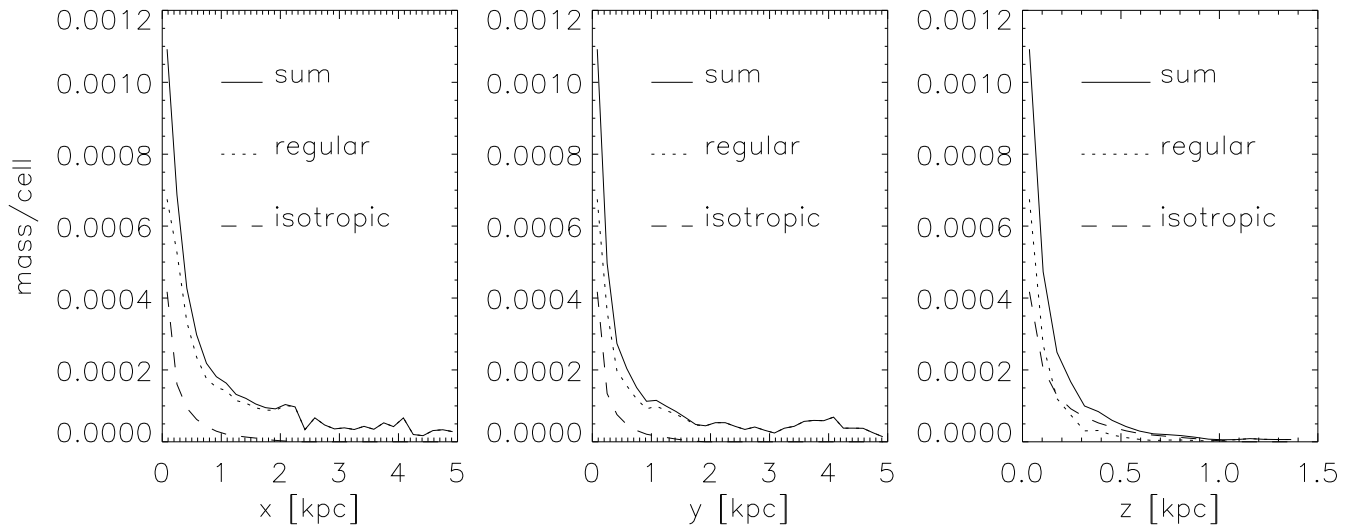


Figure 8. The mass profiles of our model are shown along the x , y and the z -axes. The isotropic DF contributes two-thirds as much mass as the regular component near the centre. Along the x -axis the contribution from the isotropic DF decreases rapidly, while along the z -axis the isotropic component becomes steadily more important until it dies out near $z \sim 1.2$. Relatively few regular orbits pass through the minor axis, so the discrepancies between our model and the input density are substantial further than 1.2 kpc down the z -axis.

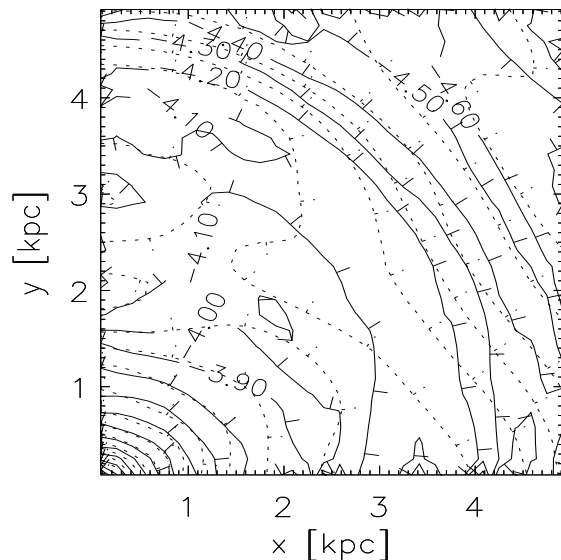


Figure 7. The mass within 0.14 kpc of the Galactic plane is shown for the Binney et al. (1997) input density (dotted contours) and for the present model (full contours). While the model can reproduce the mass in the inner parts very well it fails to reproduce the over-densities on the y -axis that are most likely due to symmetrized spiral arms.

y -axis. Outside these areas, the error is very much smaller. The model reproduces both the axis ratio and the detailed shapes of the contours in the (x, z) and (y, z) planes very well out to the limits of the box, although there are some small discrepancies on the z -axis – see below.

Fig. 7 highlights the discrepancies between the model and input densities in the (x, y) plane by contouring for each model the mass within 0.14 kpc of the plane. The two sets of contours agree well within corotation, but significant dis-

crepancies occur further out. These discrepancies are not worrying for two reasons. First, obscuration is at its worst in the Galactic plane, and in the region one cannot confidently deproject the surface photometry. Second, the deprojection algorithm of Binney et al. assumes that all structures are eight-fold symmetric with respect to the principal planes of the bar. Spiral arms are less symmetric and spurious features will arise when one attempts to deproject a spiral distribution under the assumption of eight-fold symmetry. Indeed, Binney et al. show that features remarkably like the ‘observed’ the density maxima along the y -axis arise when the Binney et al. algorithm is used to deproject a four-armed spiral distribution. Englmaier & Gerhard (1998) provide further evidence for this interpretation by showing that better fits to the observed longitude–velocity diagrams for HI and CO are obtained when the flow of gas in the inner Galaxy is calculated in a potential that includes contributions from the density maxima. Moreover, the contributions from the maxima induce a four-armed rather than a predominantly two-armed spiral in the gas. Hence several lines of evidence indicate that the density maxima in the deprojected disk are artifacts associated with four spiral arms. Such spiral arms inevitably lie beyond the reach of our modelling technique.

Fig. 8 shows density profiles of the model along the x - and z -axes. At the centre the isotropic component contributes over 30 per cent of the mass. Within the plane this component diminishes rapidly in importance as one moves away from the centre. Along the z -axis, by contrast, the isotropic component gains in importance as one moves from the centre because many of the orbits passing through the z -axis are irregular. Beyond ~ 1.2 kpc, the isotropic component is unable to contribute to the density because orbits inevitably have Jacobi energies in excess of $\Phi_{\text{eff}}^{\text{rim}}$, and the discrepancies between our model and the deprojected photometry increase.

Table 5. Model predictions for unmeasured quantities.

(ℓ, b)	v_{los}	μ_ℓ	μ_b	σ_{los}	σ_ℓ	σ_b	$C_{s\ell}$	C_{sb}	$C_{\ell b}$	Ref
$(1^\circ, -4^\circ)$		0.26	-0.01		3.5	2.8	-0.05	0.03	0.04	Sh
$(1^\circ, -4^\circ)$	3.8	0.25	-0.01				-0.05	0.03	0.04	Sp
$(8^\circ, 7^\circ)$		-0.85	-0.22		6.0	3.4	0.52	0.05	-0.14	M
$(12^\circ, 3^\circ)$		0.70	-0.10		4.4	2.1	0.08	-0.05	0.01	M
$(8.4^\circ, -6^\circ)$	77	0.87	0.29	78	3.1	3.0	0.31	-0.01	0.15	TT
$(1.21^\circ, -1.67^\circ)$	8	-0.16	-0.09	134	3.5	3.0	-0.11	0.02	0.04	Bl
$(-1.14^\circ, 1.81^\circ)$	-8	-0.20	0.01	112	4.4	2.6	-0.10	-0.01	0.03	Bl

Units are mas yr^{-1} for proper-motions and km s^{-1} for velocities. The C_{ij} are the dimensionless correlation coefficients of the observable velocity dispersion tensor, that are defined by equation (47). The first four windows are those used to constrain the model (data used for that purpose are given in Table 4 and are omitted here), the fourth window has been observed by Tiede & Tendrup (1997), and the last two by Blum et al. (1997). The line of sight streaming for the Blum et al. fields has not been corrected for the reflex motion of the Sun to enable comparison with his data.

Table 4. Kinematic data used to constrain the model.

(ℓ, b)	Quantity	observed	Model	Ref
$(1^\circ, -4^\circ)$	v_{los}	4 ± 8	4	Sh
	σ_{los}	113 ± 5	115	
$(1^\circ, -4^\circ)$	σ_{los}	120	114	Sp
	σ_ℓ	3.2 ± 0.1	3.6	
	σ_b	2.8 ± 0.1	2.8	
$(8^\circ, 7^\circ)$	v_{los}	45 ± 10	45	M
	σ_{los}	85 ± 7	80	
$(12^\circ, 3^\circ)$	v_{los}	77 ± 7	75	M
	σ_{los}	68 ± 6	95	

The units are km s^{-1} for velocity dispersions and mas yr^{-1} for proper-motion dispersion (σ_ℓ and σ_b). The last column is the mnemonic for the observers (see Table 1). The biggest discrepancies occur at $(12^\circ, 3^\circ)$, where our dynamical model has too much dispersion and not enough streaming.

6.1.2 The kinematics

It is essential to apply both photometric and kinematic constraints to obtain plausible models of the inner galaxy. The dynamical model is required to reproduce the data provided by Sharples et al. (1990) and Spaenhauer et al. (1992) in Baade’s Window, together with the observations of Minniti et al. (1992) at $(8^\circ, 7^\circ)$ and $(12^\circ, 3^\circ)$. Note that we maintain a distinction between the Sharples et al. (1990) and the Spaenhauer et al. (1992) data-sets, as the model is viewed at the same window through different selection functions. Table 4 shows how the model fares. In Baade’s Window, the line-of-sight streaming velocity, v_{los} , and velocity dispersion, σ_{los} , together with one of the proper-motion dispersions σ_b are well reproduced. The remaining proper-motion dispersion σ_ℓ is higher than measured by Spaenhauer et al. (1992). This is because our orbit library, and hence our model, probably contains too many retrograde orbits. Turning to the Minniti et al. (1992) fields, the streaming velocity and the dispersions at $(8^\circ, 7^\circ)$ are reproduced to within the error bars. The more distant window at $(12^\circ, 3^\circ)$ is more difficult to get right. One worry is that disk contamination is likely to be severe in this outer window, which may mean that Minniti et al.’s (1992) results need correction. This explanation is consistent with the fact that our model has a higher

dispersion and a lower streaming velocity than are suggested by the data. Overall, though, Table 4 encourages us in the belief that our dynamical model is a good representation of the inner Milky Way and that it is useful to make some kinematic predictions from the model.

6.2 Kinematic predictions

Let us stay for the moment with our constraint fields. In Baade’s Window, the means in the proper motions μ_ℓ and μ_b are not given by Spaenhauer et al. (1992), but it may become possible to recover them at some time in the future. The mixed components of the velocity dispersion tensor are also thus far unmeasured, although there is preliminary claim of a measurement of the vertex deviation from a small sample by Zhao, Spergel & Rich (1994). In the Minniti et al. (1992) fields, only line-of-sight quantities are available. Table 5 presents the predictions of our model for all the unmeasured quantities. [We have not given results for $(12^\circ, 3^\circ)$ because our dynamical model does not reproduce the existing data there.] We also compute the correlation coefficients between the observable velocity dispersions

$$C_{s\ell} \equiv \frac{\sigma_{\text{los},\ell}^2}{\sigma_{\text{los}} \sigma_\ell}, \quad C_{sb} \equiv \frac{\sigma_{\text{los},b}^2}{\sigma_{\text{los}} \sigma_b}, \quad C_{\ell b} \equiv \frac{\sigma_{\ell b}^2}{\sigma_\ell \sigma_b}. \quad (47)$$

Zhao, Spergel & Rich (1994) suggest that $C_{s\ell}$ is a useful diagnostic of bulge triaxiality. At Baade’s Window, this quantity vanishes for a steady-state axisymmetric density distribution. The predictions for these correlations are presented in the tables. They are, of course, measures of the misalignment of the principal axes of the velocity dispersion tensor with the (s, ℓ, b) axis set. In Baade’s Window, the dispersion tensor has principal semi-axes in the ratio $0.83 : 1 : 0.77$, with the longest axis pointing almost in the \hat{e}_ℓ direction. Hence, Baade’s Window is a rather poor place to look for the signature of triaxiality. Our barred model has a dispersion tensor whose alignment is almost the same as that of an oblate axisymmetric model! In the Minniti et al. $(8^\circ, 7^\circ)$ field, the dispersion tensor is very strongly anisotropic, with semi-axes in the ratio $0.25 : 1 : 0.50$. The long axis points almost in the \hat{e}_ℓ direction and has the high value of 238 km s^{-1} . In the model, there are more and more retrograde stars picked up as one moves further from the Galactic Centre. The velocity dispersion in the longitudinal direction rises as

the prograde and retrograde stars become present in almost equal numbers.

Now, let us see how our model fares in comparison with data for two new fields. Tiede & Terndrup (1997) present the results of a study of 189 stars in a field at $(\ell, b) = (8.4^\circ, -6.0^\circ)$. The selection criteria are described in detail in their paper but are not simple to reproduce. A crude approximation to their selection procedure is to use the generic selection function (24) with parameters $m_{\max} = 17.0$ and $m_{\min} = 12$. Tiede & Terndrup provide values for the mean extinction $A = 1.1$ and its dispersion $\sigma_A = 0.2$. They measure the line-of-sight dispersion σ_{los} of their sample to be $75 \pm 1 \text{ km s}^{-1}$. Table 5 shows the predictions of our model. Good reason for believing in the model's reliability within corotation is that this value of the dispersion is very reproduced. The diagonalised tensor has semi-axis ratios $0.42 : 1 : 0.92$ and is rather strongly misaligned with the (s, ℓ, b) axis set, as the large correlation $C_{s\ell}$ indicates.

Blum et al. (1994) studied stars in two fields very close to the Galactic Centre at $(1.21^\circ, -1.67^\circ)$ and at $(-1.14^\circ, 1.81^\circ)$. The stars comprising the sample were selected in a manner that tried to exclude disk stars. It is not so easy to reproduce their selection procedure. A crude approximation is to take the selection function as unity for all heliocentric distances s satisfying $6 \text{ kpc} < s < 10 \text{ kpc}$. From their data, Blum et al. deduce that $v_{\text{los}} = 14 \pm 23 \text{ km s}^{-1}$ and $\sigma_{\text{los}} = 128 \pm 14 \text{ km s}^{-1}$ at $(1.21^\circ, -1.67^\circ)$ and that $v_{\text{los}} = -75 \pm 24 \text{ km s}^{-1}$ and $\sigma_{\text{los}} = 127 \pm 17$ at $(-1.14^\circ, 1.81^\circ)$. The predictions of our model for these two new fields are reported in Table 5. Again, there is the reassuring circumstance that both the dispersions are reproduced to within the errors. One of the streaming velocities is recovered to within the error bars, but one is not. At $(1.21^\circ, -1.67^\circ)$ the dispersion tensor has semi-axes $(141, 126, 112) \text{ km s}^{-1}$, while at $(-1.14^\circ, 1.81^\circ)$ the semi-axes are $(111, 167, 100) \text{ km s}^{-1}$. In both cases the principal axes are not strongly misaligned with the (s, ℓ, b) coordinate directions, so, as in Baade's Window, triaxiality will be hard to establish unambiguously in these fields.

Finally, Figs. 9 to 10 show the kind of kinematic data that may become available in the very near future. Here, we have imagined that our dynamical model is observed through four windows using the generic selection function (24) with a width of one magnitude. We assume that the extinction and intrinsic magnitude of the stellar population vanish, so m_{\max} is in effect the maximum distance modulus in the sample. It is apparent from Figs. 9 to 10 that a wealth of additional information is uncovered when the kinematics is studied as a function of apparent magnitude.

As one application of the figures, let us examine how to improve the slight discrepancies between the model and the observations in the constraint fields. The quantity σ_b is too large by a factor of ~ 5 per cent in Baade's Window. From Fig. 9, it is evident that this can be corrected by slightly increasing the faint cut-off, as the curve of σ_b versus m_{\max} falls for $m_{\max} > 14.5$. If, for example, either the total extinction or the faint cut-off is less severe than we have assumed, then σ_b is lowered to give better agreement with the Spaenhauer et al. data. The quantity σ_ℓ is also slightly too large in our dynamical model, but Fig. 9 makes it clear that increasing the faint magnitude cut-off makes little difference to its value. Some of the properties of the curves in Figs. 9 and 10

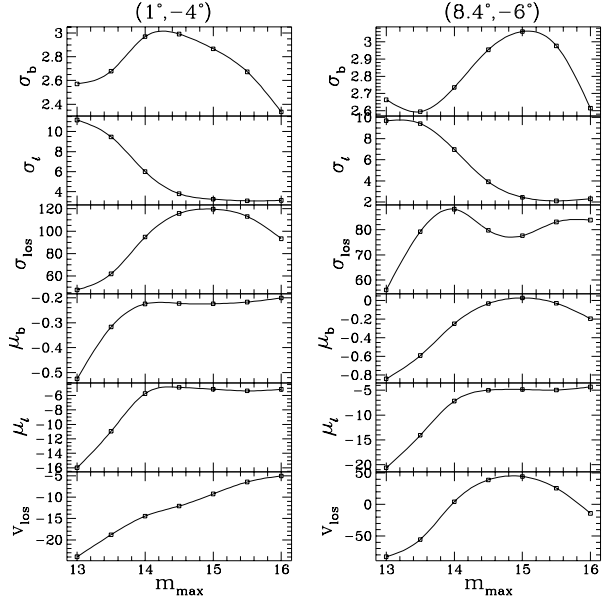


Figure 9. The left panel gives the kinematic predictions at Baade's Window ($1^\circ, -4^\circ$) and the right panel at the field studied by Tiede & Terndrup ($8.4^\circ, -6.0^\circ$). Here, the generic selection function is used with $m_{\min} = m_{\max} - 1$.

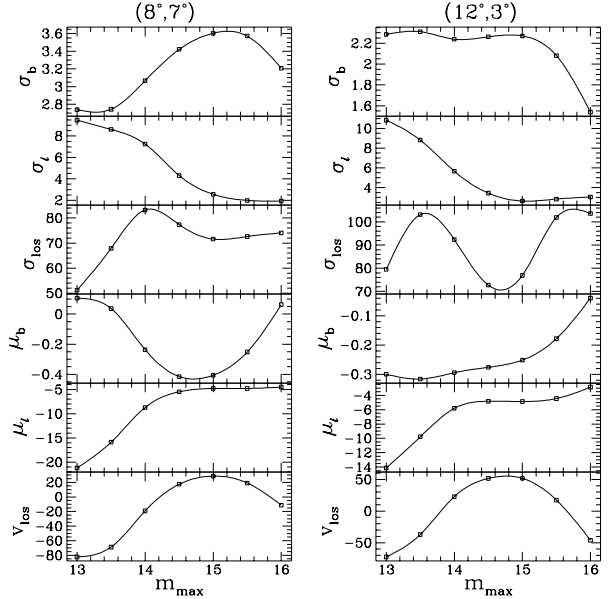


Figure 10. Kinematic predictions at Minniti et al.'s windows. The left panel shows results for $(8^\circ, 7^\circ)$, the right panel for $(12^\circ, 3^\circ)$. Again, the generic selection function is used with $m_{\min} = m_{\max} - 1$.

are readily explained. The line-of-sight streaming v_{los} typically gives a one-humped curve, as it is greatest when stars are picked up by the selection function at roughly the tangent point. The line-of-sight dispersion σ_{los} can sometimes give complex curves, as in the $(12^\circ, 3^\circ)$ field of Minniti et al. Here, as we move along the line of sight, the selection

Figure 11. The distribution function of the regular component of the final model is shown projected into the $\langle L_z \rangle / L_c - \langle E \rangle$ plane. The phase-space density is largest in the bottom left corner of the figure, which is occupied by small, nearly harmonic box orbits. At higher energies the density peaks along the ridge of the prograde x_1 -orbit family.

Figure 12. The distribution of the regular component’s mass within the $\langle L_z \rangle / L_c - \langle E \rangle$ plane. The colour of each cell encodes the sum of the weights assigned to the orbits that lie in that cell.

function picks up first a mixture of prograde and retrograde stars in the near side of the disk, then mainly prograde stars in the bar proper, and finally prograde and retrograde stars in the far side of the disk. This causes σ_{los} to rise, then fall, and then rise again.

Clearly, as sample sizes increase, it will become increasingly inappropriate to characterize the kinematics of a given field by just mean velocities and dispersions. Even observations of external galaxies can now deliver other measures of the line-of-sight velocity distribution (LOSVD), such as the Gauss-Hermite coefficients h_3 and h_4 . Still richer information should be available in the case of the Milky Way because, by varying m_{min} and m_{max} , we can probe the LOSVD at different points along the line of sight. More sophisticated data sets will surely resolve much of the degeneracy that now plagues dynamical models.

6.3 The distribution function

Fig. 11 shows the distribution function of the regular component of the final model projected onto a plane whose axes are averaged energy $\langle E \rangle$ and averaged angular momentum $\langle L_z \rangle$, normalized by the reference value, L_c , that is defined by equation (33). The phase-space density is highest at bottom left, and decreases with increasing energy for both prograde and retrograde orbits. These trends are in the same sense as the variation of f^{iso} , which decreases monotonically as H increases from bottom left to top right.

Fig. 12 shows the distribution of the mass of the regular component within the $(\langle L_z \rangle, \langle E \rangle)$ plane: the colour of each pixel encodes the sum of the weights w^{reg} assigned to orbits whose effective integrals place them within that pixel. [Equation (13) shows that the mass on an orbit is proportional to its weight.] Comparing Figs. 11 and 12 we see that mass is concentrated at much larger energies than phase-space density. This is a simple reflection of the fact that the amount of phase-space volume that is associated with a pixel in Figs. 11 and 12 increases rapidly with $\langle E \rangle$. The surprising feature of Fig. 12 is large concentration of mass in the top right corner of the diagram. This mass is on retrograde orbits around corotation. It lies there because at these effective energies the isotropic component cannot contribute, and there is a lack of regular prograde orbits.

We find that 75 per cent of the mass in the box is on orbits that are confined to be inside corotation. Of these, about a sixth (12 per cent) are in the isotropic component, half (37 per cent) are prograde regular and a third (26 per cent of the total in the box) are retrograde regular. Thus Within corotation, it is prograde orbits that are dominant.

Table 6. Mass and optical depth towards Baade’s Window (BW) and the Galactic Centre (GC).

component	mass	Sources by comp.		Lenses by comp.	
		GC	BW	GC	BW
isotropic	0.12	$1.1 \cdot 10^{-5}$	$1.1 \cdot 10^{-6}$	$3.5 \cdot 10^{-6}$	$3.6 \cdot 10^{-7}$
prograde	0.32	$2.3 \cdot 10^{-5}$	$1.3 \cdot 10^{-6}$	$2.9 \cdot 10^{-6}$	$5.1 \cdot 10^{-7}$
retrograde	0.39	$4.6 \cdot 10^{-5}$	$2.0 \cdot 10^{-6}$	$3.9 \cdot 10^{-6}$	$2.7 \cdot 10^{-7}$
hot	0.17	$1.3 \cdot 10^{-5}$	$1.3 \cdot 10^{-6}$	$9.4 \cdot 10^{-6}$	$1.1 \cdot 10^{-7}$
total	1.00	–	–	$2.0 \cdot 10^{-5}$	$1.2 \cdot 10^{-6}$

The prograde, retrograde, and hot components refer to the regular orbits with $\langle L_z \rangle / \langle (L_z - \langle L_z \rangle)^2 \rangle^{1/2}$ smaller than -3 , larger than 3 , or in between. The relative masses only refer to the contributions inside our box of $10 \times 10 \times 2.8$ kpc. The left columns give for the *sources* drawn from the various components, while the *lenses* are taken from the entire model (inside the box). The rightmost two columns are for sources throughout the model and lenses in individual components.

We have tried and failed to build models that place a much larger fractions of mass on the isotropic component. Inside corotation, chaotic orbits play quite a small role, although, as Fig. 8 illustrates, they are indispensable along the minor axis. Outside corotation, retrograde orbits dominate the mass budget. The second column of Table 6 gives the mass contained in each component.

Fig. 13 gives an overview of the distribution of mass between the various components by plotting dM/dE , the mass per unit increment in energy. Since the DF of the isotropic component is a function $f^{\text{iso}}(H)$ of the Hamiltonian, calculating the corresponding form of dM/dE involves determining the volume in phase space within which both $E(\mathbf{w})$ and $H(\mathbf{w})$ lie within specified ranges, and then multiplying this volume by f^{iso} and integrating over all H . Details of this calculation are given in Appendix C. The long-dashed curve in Fig. 13 shows the resulting curve, which rises fairly steadily with E until it drops sharply to zero as the cutoff at $H = \Phi_{\text{eff}}^{\text{rim}}$ cuts in.

The full curve in Fig. 13 shows dM/dE for the regular component in the approximation that each orbit contributes mass only to the energy that is equal to $\langle E \rangle$, the time-average of $E(\mathbf{w})$ along the orbit. Since E generally does not vary greatly along a regular orbit, this is a good approximation. Comparing the full and long-dashed curves in Fig. 13, we see that inside corotation the regular and isotropic components make comparable contributions to the overall mass, with the isotropic component dominant at the lowest energies, and the regular component mostly dominant further out. The short-dashed and dotted curves in Fig. 13 show the contributions to the regular component from prograde and retrograde orbits, respectively. Prograde orbits generally contribute more than half the mass. Around the corotation energy, $E = -0.05$, there is a glaring exception to this rule, however, as the contributions to dM from prograde orbits plunges to zero and retrograde orbits provide all the mass. At slightly higher energies the relative importance of the two orbit types reverses, sharply.

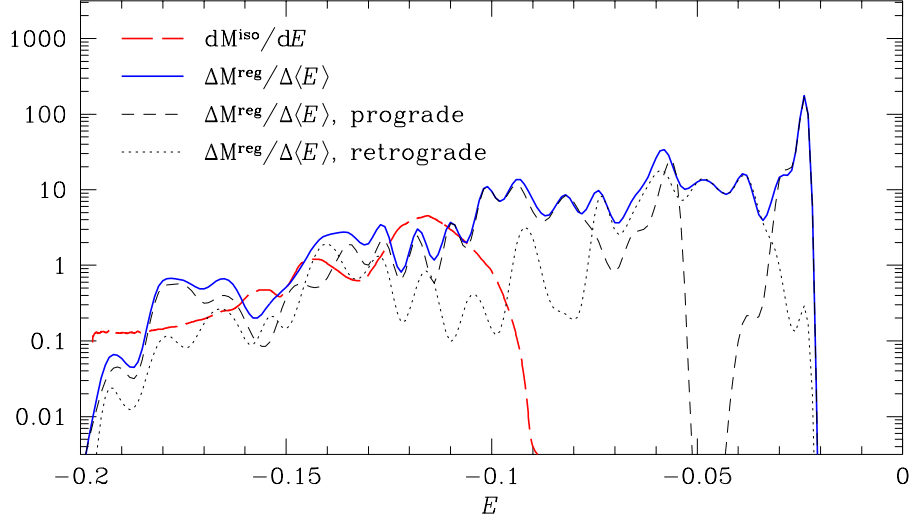


Figure 13. The differential mass distribution of the isotropic and the regular component. The regular part is further split into prograde and retrograde orbits. The isotropic component stops rather abruptly at $E = -0.09$ since it is confined to inside corotation.

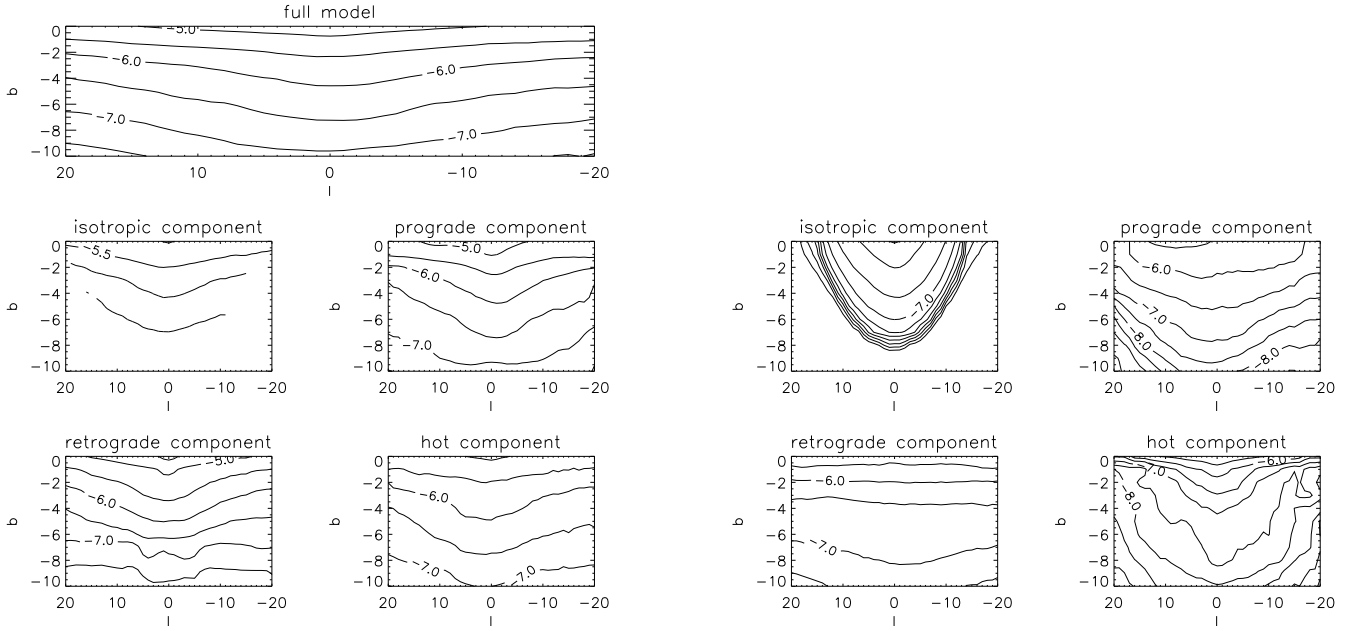


Figure 14. Logarithmic (to the base 10) contours of the microlensing optical depth for $\beta = 0$. **Left:** lenses drawn from the full model while the source population differs from panel to panel; this corresponds to the results on the left part of Table 6. **Right:** sources drawn from the full model while the lens population differs from panel to panel. Note that the density, and hence the optical depth, of the component with the isotropic DF ends abruptly at corotation.

6.4 The microlensing optical depth

The optical depth for gravitational microlensing, τ , is given by

$$\tau = \frac{4\pi G}{c^2} \frac{\int_0^\infty dD_s \frac{D_s^2 \rho_s(D_s)}{D_s^{2\beta}} \int_0^{D_s} dD_d \frac{D_d (D_s - D_d) \rho_d(D_d)}{D_s}}{\int_0^\infty dD_s \frac{D_s^2 \rho_s(D_s)}{D_s^{2\beta}}}. \quad (48)$$

Here, the subscripts d and s refer to deflector and source objects, respectively and β parameterizes the efficiency with which stars are picked up along the line of sight (see e.g., Kiraga & Paczyński 1994). The value $\beta = 0$ is appropriate for sources luminous enough to be included in a microlensing survey no matter how far away they lie within the Galaxy, while $\beta = 1$ is appropriate for less luminous sources that have a probability of being included in the survey that falls off with heliocentric distance s as s^{-1} . Typically, $\beta = 0$ is appropriate for red-clump stars, while $\beta \approx 1$ is appropriate for main-sequence stars. The top left panel of Fig. 14 shows contours of optical depth for the case $\beta = 0$, while the

bottom entries in the last two columns of Table 6 give numerical values for the direction towards the Galactic centre and Baade’s Window. These depths are only for microlensing a source that lies within the box by a lens that also lies within the box. Hence, before they are compared with observations, these numbers should be augmented by the contribution from the foreground disk, which for Baade’s Window typically amounts to $0.1 - 0.3 \times 10^{-6}$ (e.g., Evans 1995). The augmented value for Baade’s Window, namely 1.4×10^{-6} , is smaller than the observational value: Udalski et al. (1994) found $\tau = (3.3 \pm 1.2) \times 10^{-6}$ for clump stars, while Alcock et al. (1997) found $\tau = (3.9^{+1.8}_{-1.2}) \times 10^{-6}$ for clump stars near to Baade’s Window. This problem was discussed in detail by Bissantz et al. (1997), who examined essentially the input density distribution.

The four right-hand panels of Fig. 14 and the other entries in the last two columns of Table 6 break the overall optical depth down into contributions from individual components. Towards the Galactic centre, the largest contribution comes from lenses in the hot component, while in Baade’s Window this component makes the smallest contribution because of its high degree of central concentration. Nearly half the overall optical depth in Baade’s Window comes from lenses in the prograde component.

The four lower left panels in Fig. 14 and the second and third columns of Table 6 give the optical depth values when the lenses are drawn from the full model, but the sources are separated by component. The table shows that these vary by a factor of up to 2 in a given direction. Specifically, in Baade’s window, sources that move on retrograde orbits are nearly twice as likely to be lensed as sources that belong to the isotropic component, and, in fact, have an optical depth that is compatible with the measurement of Udalski et al. The origin of this phenomenon is simple: objects that lie near the outside of the box, but diametrically opposite to the Sun, inevitably have larger optical depths than objects at the Galactic centre. Fig. 13 shows that the largest radii are dominated by retrograde orbits, while the isotropic component is concentrated at the centre. There is a real possibility that the density of clump stars does not rise towards the Galactic centre as rapidly as the overall stellar mass density, with the result that their optical depth is anomalously high like that of the model’s retrograde objects.

Barred models can possess asymmetric microlensing maps (Evans 1994, Zhao & Mao 1996). Two competing effects can be discerned in Fig. 14. First, lines of sight to sources at negative longitudes are longer and pass through more of the dense central bulge than lines of sight at positive longitudes. This is because the sources at negative longitudes are on average further away. Second, the selection effect, controlled by the parameter β , can enhance the optical depth at positive longitudes rather than negative, as here the sources appear to be brighter. These two effects tend to work against each other, so the final asymmetry of the map is a subtle matter. For example, in the panel on the extreme right of the middle row of Fig. 14, which is for lenses that lie in the prograde component and sources that are drawn from the full dynamical model, we see enhanced optical depths at negative longitudes, but only outside the plane. Within the plane, any interpretation is difficult because this is where our dynamical model is least reliable. By contrast, when the sources lie in the retrograde component

near the Galactic plane (extreme left panel of bottom row of Fig. 14), the asymmetry goes the other way. Here, the main contribution is from sources at the far end of the Galaxy outside corotation, and now the optical depth is enhanced if the lenses lie roughly halfway between observer and source. This favours positive longitudes, as there is a ready supply of such lenses in the foreground bar.

From the top-left panel of Fig. 14 we see that the optical depth is always larger at negative longitudes when $|b| > 1^\circ$. The coming decade is likely to see the gradient of microlensing optical depth with Galactic longitude and latitude measured, at least at certain spots in the Bulge. For example, the third panel from the left in the bottom row of Fig. 14 shows that when the lenses are drawn from the retrograde component, the gradient with respect to Galactic longitude near the plane is negligible, although the latitudinal gradient remains steep. At on-axis ($b \sim 0^\circ$) fields with $\ell > 10^\circ$, the optical depth is mainly provided by the retrograde component. Hence, gradient information, by giving an indication of the shape of the contours in the microlensing maps, may provide clues as to which components are providing the largest numbers of sources and lenses.

7 CONCLUSIONS

We have shown how Schwarzschild’s method can be used to produce models with known DFs. Previously, models constructed by Schwarzschild’s (1979) method have had known DFs only when the DF depended only on classical integrals (e.g., Cretton et al. 1999). The great merit of Schwarzschild’s method is precisely its ability to handle the general case in which non-classical integrals are important, so our algorithm for determining the DF of a general model must be counted a significant advance.

One advantage of being able to determine the DF of a Schwarzschild model is that one can then combine a crude approximation to the galaxy with a DF that depends only on classical integrals, with a more general DF obtained by Schwarzschild’s method. In this approach, only the difference between the true DF and the classical DF need be reproduced with orbits. The resulting model will have higher resolution in real- and velocity-space, and be easier to interpret physically than one constructed by the classical Schwarzschild technique.

A key point is that when a classical DF is used in the construction of a Schwarzschild model, the weights of orbits can be negative because the orbits may be subtracted from the underlying classical component, subject only to the constraint that the total phase-space density is non-negative. When regular orbits are assigned negative weights, these orbits are important because they are excluding stars on chaotic orbits from certain regular parts of phase space.

We have illustrated these new techniques by using them to construct a model of the central kiloparsecs of the Milky Way. This problem is less well suited to the new techniques than the classical problems of modelling axisymmetric systems and triaxial systems with negligible figure rotation because there is only one classical integral, the Jacobi energy, and this integral is not confining for the more energetic stars. Moreover, the phase space of the inner Galaxy is more chaotic than regular, and Schwarzschild’s technique

works best in a highly regular phase space. From the fact that we have succeeded in constructing a reasonable model of the inner Galaxy notwithstanding these difficulties, we infer that the new techniques would solve easier classical problems with some facility.

Our new Galaxy model reproduces essentially all of the available density and kinematic data within corotation (~ 3.6 kpc). In particular, the three-dimensional bar density of Binney et al. (1997) is faithfully reproduced in the inner parts. At corotation, our dynamical model does not reproduce the over-densities on the minor axis found by Binney et al. – but these are probably artifacts of the deprojection algorithm, which assumes that the underlying model is eightfold symmetric and must misrepresent spiral features. The kinematic data in Baade’s Window ($1^\circ, -4^\circ$) and in the field studied by Minniti et al. (1992) at ($8^\circ, 7^\circ$) are all fitted to within the observational uncertainties. The model does not fit data for the outer window of Minniti et al. (1992) at ($12^\circ, 3^\circ$) accurately in that it has a higher line-of-sight dispersion and a lower streaming velocity than the data. This mismatch may be caused by disk contamination in the Minniti et al. sample or by too low an assumed value for the mean extinction in our model.

In addition to fitting the initially prescribed data, the model furnishes many predictions. We have tested a few of these predictions against data in the literature and find that they are consistent with measurements by Blum et al. (1994) at ($1.21^\circ, -1.67^\circ$) and ($-1.14^\circ, 1.81^\circ$), and by Tiede & Terndrup (1997) at ($8.4^\circ, -6^\circ$). For several well studied fields we predict values for quantities, such as proper-motion dispersions, that have not yet been measured. We find that in central fields, such as Baade’s Window, the principal axes of the velocity-dispersion tensor tend to be approximately aligned with the line of sight. Hence, these are not good locations to probe for kinematic signatures of triaxiality.

The most puzzling aspect of our model is its reliance on retrograde orbits in a narrow band of energies, that corresponds to radii around 3 kpc. This fact has an observationally testable consequence: at ($8^\circ, 7^\circ$) the dispersion tensor should be extremely anisotropic, with its longest axis aligned nearly with the \hat{e}_ℓ direction, because samples should contain roughly equal numbers of prograde and retrograde stars, on roughly circular orbits. Is this counter-intuitive prediction an artifact of our model or a robust prediction? It is a consequence of two inputs: (i) the density profile of Binney et al., and (ii) the decision to exclude from the orbit library orbits with Liapunov times shorter than five bar rotation periods.

The density distribution of Binney et al. is very uncertain at the relevant radii by virtue of a combination of the effects of spiral structure and obscuration. Photometry of external barred galaxies, such as NGC 1300 (Elmegreen et al. 1996) suggests that the Binney et al. profile may be significantly in error, and that the density should drop steeply inside corotation to a lower, approximately level value that extends throughout the highly chaotic region around corotation. An approximately constant density around corotation could be provided by prograde orbits that have apocentres well outside corotation. By specifying a density gradient around corotation, we have obliged the fitting algorithm to employ orbits with apocentres at smaller radii, and the only available regular orbits are retrograde. Alternatively, we may

have been too conservative in our criterion for excluding orbits as chaotic: an orbit that has a short Liapunov time may never the less remain trapped for a substantial fraction of a bar rotation period. In a subsequent study it would be interesting to use the spectral approach to determining orbital regularity (Binney & Spergel 1984; Carpintero & Aguilar, 1998) instead of Liapunov exponents, which are expensive to compute and may be more misleading in cases of mild stochasticity. Moreover, even though half of all disk galaxies have bars, it is not clear that any individual bar lives for a Hubble time; bars may dissolve and reform on a shorter timescale.

We have calculated microlensing maps for our model. These show that the overall microlensing optical depth of luminous sources in Baade’s window is at least a factor 2 smaller than the observations require. They show also that sources in different components have optical depths that differ by up to a factor 2. Hence, it is important to characterize the populations to which stars that are known to have been lensed belong, and to understand the mix of populations that characterizes the stars that are regularly monitored for microlensing events. In principle, our model allows one to determine the distribution of durations of the lensing events in any field, and we plan to present such distributions shortly.

It would be useful to extend the work in this paper by building dynamical models for different bar morphologies, viewing angles and pattern speeds. However, our experiments have convinced us that there is very considerable freedom to reproduce the existing data by superposition of orbits. This means that restricting the viewing angle from the stellar kinematics alone will be challenging.

To meet this challenge, more kinematic data in the inner Galaxy are urgently needed. It may well be possible to extract more information by studying the variation of kinematic quantities with distance along the line of sight using well-defined selection functions. For external galaxies, where all stars are at roughly the same distance from the observer, it makes sense to record a single number for a kinematic quantity like the velocity dispersion along the line of sight. In studies of the Milky Way, this approach fails to exploit the full richness of information that is available to us. It would be more fruitful to calculate the kinematic quantities for stars in the sample with, for example, magnitudes between m_{\max} and $m_{\min} = m_{\max} - 1$. As we have shown for the dynamical model, there are interesting and useful variations of kinematic quantities with m_{\max} . These will prove invaluable in elucidating the structure of the bar, since the photometry together with the available line-of-sight dispersions and streaming velocities are not enough to prescribe the bar uniquely.

ACKNOWLEDGMENTS

RMH and WD acknowledge financial support from PPARC, while NWE is supported by the Royal Society. We thank Ortwyn Gerhard and Hongsheng Zhao for helpful discussions.

REFERENCES

Alcock et al., 1997, ApJ, 479, 119

- Binney J.J., Gerhard O.E., Stark A.A., Bally J., Uchida K.I. 1991, MNRAS, 252, 210
- Binney J.J., Gerhard O.E., Spergel D.N. 1997, MNRAS, 288, 365
- Binney J., Merrifield M. 1998, Galactic Astronomy, (Princeton University Press, Princeton)
- Binney J., Spergel D.N., 1984, MNRAS, 206, 159
- Binney J., Tremaine S., 1987, Galactic Dynamics, (Princeton University Press, Princeton)
- Bissantz N., Englmaier P., Binney J.J., Gerhard O.E., 1997, MNRAS, 289, 651
- Blitz L., Spergel D.N., 1991, ApJ, 379, 631
- Blum R.D., Carr J.S., DePoy D.L., Sellgren K., Terndrup D.M. 1994, ApJ, 422, 111
- Carpintero D.D., Aguilar L.A., 1998, MNRAS, 298, 1
- Cretton N., de Zeeuw P.T., van der Marel R.P., Rix H.-W., 1999 astro-ph/9902034
- de Vaucouleurs G. 1964, In: IAU Symposium 20, The Galaxy and the Magellanic Clouds, eds F. Kerr, A. Rodgers, p. 195 (Australian Academy of Sciences, Canberra)
- Elmegreen B.G., Elmegreen D.M., Chromey F.R., Hasselbacher D.A., Bissell B.A., 1996. AJ 111 2233
- Englmaier P., Gerhard O.E. 1998, MNRAS, submitted
- Evans N.W., 1994, ApJ, 437, L31
- Evans N.W., 1995, ApJ, 445, L105
- Kuijken K., Dubinski J. 1995, MNRAS, 277, 1341
- Lake G., Norman C., 1983, ApJ, 270, 51
- Merritt D., Fridman T. 1996, ApJ, 460, 136
- Minniti D., White S.D.M., Olszewski E.W., Hill J.M. 1992, ApJ, 393, L47
- Newton, A.J., Binney, J.J., 1984, MNRAS, 210 711
- Paczyński B., et al., 1994, ApJ, 435, L113
- Pfenniger D. 1984, AA, 134, 373
- Pfenniger D., Friedli D. 1991, AA, 252, 75
- Press W.H., Flannery B.P., Teukolsky S.A., Vetterling W.T. 1988, Numerical Recipes, chap. 10, (Cambridge University Press, Cambridge)
- Rich R.M. 1988, ApJ, 95, 828
- Schwarzschild M. 1979, ApJ, 232, 236
- Schwarzschild M. 1982, ApJ, 263, 599
- Schwarzschild M. 1993, ApJ, 409, 563
- Sellwood J.A. 1993, In: Back to the Galaxy, The Third Maryland Conference, eds S.S. Holt, F. Verter (American Institute of Physics, New York)
- Sevenster M., Saha P., Valls-Gabaud D., Fux R. 1998, MNRAS, in press
- Sharples R., Walker A., Cropper M. 1990, MNRAS, 246, 54
- Spaenhauer A., Jones B.F., Whitford A.E. 1992, AJ, 103, 297
- Spergel D.N., Malhotra S., Blitz L. 1996, In: Spiral Galaxies in the Near-InfraRed, eds D. Minniti, H-W. Rix (Springer-Verlag, Berlin).
- Stanek K. 1996, ApJ, 460, L37
- Stoer J., Bulirsch R. 1980, Introduction to Numerical Analysis, (Springer-Verlag, New York)
- Statler T.S. 1987, ApJ, 321, 113
- Terndrup D.M., Sadler E.M., Rich R.M., 1995, AJ, 110, 1774
- Tiede G.P., Terndrup D.M., 1997, AJ, 113, 321
- Udalski A. et al., 1994, Acta Astron., 44, 165
- Zhao H.S., 1996, MNRAS, 283, 149
- Zhao H.S., Mao S., 1996, MNRAS, 283, 1197
- Zhao H.S., Spergel D.N., Rich R.M., 1994, AJ, 283, 149

APPENDIX A: NUMERICAL ALGORITHM FOR THE POTENTIAL

This appendix sketches the calculation of the potential for the Binney et al. (1997) bar density. A straightforward ex-

pansion in spherical harmonics converges rather slowly, especially in the flat disk component. However, this problem can be overcome by a technique due to Kuijken & Dubinski (1994). Given a disk with density $\rho = f(R)h(z)$, the potential is written as $\Phi = \tilde{\Phi} + f(r)H(z)$, where r denotes spherical radius and $H(z)$ is uniquely determined by $H''(z) \equiv h(z)$ and $H(0) = H'(0) = 0$ (primes denoting derivatives). Inserting this into Poisson's equation gives

$$\frac{\nabla^2 \tilde{\Phi}}{4\pi G} = [f(R) - f(r)]h(z) - f''(r)H(z) - \frac{2f'(r)}{r} [H(z) + zH'(z)]. \quad (\text{A1})$$

The expression on the right hand side is zero at $z = 0$. The mass density generating $\tilde{\Phi}$ is not strongly flattened, so that it can be economically evaluated by, e.g., multipole expansion. Here, this technique is used for the two sub-disks. The subsequently evaluated potential $\tilde{\Phi}$ and the modified density is then expanded in spherical harmonics up to order $l_{\max} = 64$. The sharp truncation of this expansion at l_{\max} causes unphysical ringing of the resulting density and in order to suppress this we have tapered the density expansion by multiplying it with $\exp(-[l/32]^2)$. Finally, the potential and resulting forces have been computed on a pseudo-Cartesian $101 \times 101 \times 161$ grid of size $20 \text{ kpc} \times 20 \text{ kpc} \times 18 \text{ kpc}$. The points are linear in $2 \ln(1+x/2)$, $2 \ln(1+y/2)$, and $\ln(1+2z)/2$. Potential and forces are then evaluated via a fifth order three dimensional spline. At each grid point, this spline gives the stored values of potential and its derivatives. The forces have everywhere continuous first and second derivatives. In particular, the interpolated forces agree identically with derivatives of the interpolated potential, as is necessary if the Jacobi energy is to be accurately conserved along numerically integrated orbits. The evaluation of potential and forces is quick once the spline coefficients have been pre-computed.

APPENDIX B: CALCULATION OF THE SECOND VELOCITY MOMENTS

This appendix briefly sketches how to calculate the second moments for the regular and isotropic parts of the DF in turn.

B1 Regular part of DF

To compute a velocity moment projected along the line of sight towards (ℓ_0, b_0) with the formalism of Section 2.4, we define

$$\hat{\Pi}(\mathbf{w}) \equiv \delta(\ell - \ell_0) \delta(b - b_0) \epsilon(s) g(\mathbf{w}). \quad (\text{B1})$$

where $g(\mathbf{w})$ is determined by the velocity moment in question. For example, to obtain v_{los} , one takes $g = \mathbf{p} \cdot \hat{\mathbf{s}}$, where $\hat{\mathbf{s}}$ is the unit vector in direction of the line of sight. With this choice, one obtains for the projected moment using equations (9) to (11)

$$\Pi[f^{\text{reg}}] = \frac{1}{N^s} \sum_i^{N^{\text{reg}}} w_i^{\text{reg}} \lim_{T \rightarrow \infty} \frac{1}{T} \int_0^T dt \epsilon(s_i(t)) g(\mathbf{w}_i(t)) \times \tilde{\delta}(\ell_i(t) - \ell_0) \tilde{\delta}(b_i(t) - b_0) \quad (\text{B2})$$

Here, $\tilde{\delta}(x)$ denotes a “ δ -function” of some finite width, which in Baade's Window, for example, is $30'$. The reason that we

cannot use strict δ -functions is that the probability for any single orbit to hit the line of sight in our finite integration interval of 200 dynamical times is zero. That is, the need for the finite-width functions $\tilde{\delta}$ arises because we replaced (i) the integral over action-space by a finite sum (by virtue of the Monte-Carlo method), and (ii) the integral over angles by a finite, rather than infinite, time integral.

B2 Isotropic part of DF

Computing moments of the isotropic part of the DF f^{iso} can be done directly since f^{iso} is explicitly given as a function of Jacobi energy E_J and therefore phase-space coordinates \mathbf{w} . The projected luminosity density is

$$\nu(\ell, b) = 4\pi \int ds s^2 \epsilon(s) \int dv v^2 f(\mathbf{r}(s, \ell, b), \mathbf{v}). \quad (\text{B3})$$

The second integral can be performed analytically for the second order splines $B_i(E_J)$ that constitute the building blocks of f^{iso} – see equation (37). The integration over s is done numerically.

Since E_J depends only on the modulus of the velocity (and not \mathbf{v} itself), the first moments $\int d\mathbf{v} \mathbf{v} f^{\text{iso}}$ vanish and one obtains $\langle v_i \rangle = -v_{\odot i}$, i.e. the solar motions, while

$$\langle \mu_i \rangle = -\frac{v_{\odot i}}{\nu(\ell, b)} \int ds s^2 \epsilon(s) \frac{\rho^{\text{iso}}(\mathbf{r})}{s} \quad (\text{B4})$$

which is just the solar reflex motion $v_{\odot i}/s$ weighted by the density along the line of sight. For the second velocity moments one finds ($p \equiv |\mathbf{p}|$)

$$\nu \sigma_{ij}^2 = \delta_{ij} \frac{4\pi}{3} \int ds s^2 \epsilon(s) \int dp p^4 f^{\text{iso}}(\mathbf{r}(s, \ell, b), p), \quad (\text{B5})$$

where the inner integral can be performed analytically by the aid of

$$\int dp p^4 B_i(E_J) = \frac{8\sqrt{2}k_i}{35\Delta E_J} [D_{i-1}^7 - 2D_i^7 + D_{i+1}^7] \quad (\text{B6})$$

with $D_i^2 \equiv E_{J_i} - \Phi_{\text{eff}}(\mathbf{r})$. The outer integral is performed numerically. For dispersions involving proper motions rather than velocities, one has to change the integrand by factors of s^{-1} .

APPENDIX C: DIFFERENTIAL MASS IN THE ISOTROPIC COMPONENT

We want to calculate the differential mass dM/dE , where E denotes the energy, for the isotropic part $f^{\text{iso}}(E_J)$ of the distribution function. Let us consider a δ -function at $E_J = E_{J0}$, then its contribution to dM/dE at $E = E_0$ is simply the volume of the four-dimensional cross-section of the phase-space hyper-planes at $E_J = E_{J0}$ and $E = E_0$

$$g(E_0|E_{J0}) \equiv \int d^6\mathbf{w} \delta(E_J - E_{J0}) \delta(E - E_0). \quad (\text{C1})$$

Then

$$\frac{dM}{dE} = M_{\square} \int dE_J g(E|E_J) f^{\text{iso}}(E_J), \quad (\text{C2})$$

i.e. g is the density of states at given E_J . With $d^3\mathbf{p} = 2\pi R^{-1}dE dL_z$ (after integrating out one angle in \mathbf{p} -space) and $E_J = H - \Omega L_z$ (equation 15) (C1) becomes

$$\begin{aligned} g(E_0|E_J) &= \frac{2\pi}{\Omega} \int \frac{d^3\mathbf{r}}{R} \int_{\Phi(\mathbf{r})}^{\Phi(\infty)} dE \delta(E - E_0) \\ &\quad \times \int_{-R\sqrt{2(E-\Phi)}}^{+R\sqrt{2(E-\Phi)}} dL_z \delta\left(L_z - \frac{E-E_J}{\Omega}\right) \\ &= \frac{2\pi}{\Omega} \int d\phi \int dz (R_2 - R_1). \end{aligned} \quad (\text{C3})$$

Here, $R_{1/2}(E_0, E_J, z, \phi)$ are the roots of

$$(E_0 - E_J)^2 = 2R^2\Omega^2(E_0 - \Phi(R, z, \phi)), \quad (\text{C4})$$

more precisely, the minimum of these roots and the corotation radius – recall that the isotropic component lives only inside corotation.

This figure "Feb99.df.reg.gif" is available in "gif" format from:

<http://arXiv.org/ps/astro-ph/9905086v1>

This figure "Feb99.mass.reg.gif" is available in "gif" format from:

<http://arXiv.org/ps/astro-ph/9905086v1>

This figure "Liap.gif" is available in "gif" format from:

<http://arXiv.org/ps/astro-ph/9905086v1>

This figure "Orbits.pro.retro.gif" is available in "gif" format from:

<http://arXiv.org/ps/astro-ph/9905086v1>

This figure "Unity.mass.gif" is available in "gif" format from:

<http://arXiv.org/ps/astro-ph/9905086v1>